Master Thesis

Properties of dissipatively coupled optomechanical systems

Talitha Weiß

12.12.2012
(revised: 29.04.2013)

Department of Physics, University of Basel
Klingelbergstrasse 82, 4056 Basel, Switzerland

Supervisor: Dr. A. Nunnenkamp
Prof. Dr. C. Bruder

Formular drucke

Philosophisch-Naturwissenschaftliche Fakultät
der Universität Basel
Dekanat

Erklärung zur wissenschaftlichen Redlichkeit
(beinhaltet Erklärung zu Plagiat und Betrug)

(bitte ankreuzen)
☐ Bachelorarbeit
☒ Masterarbeit

Titel der Arbeit *(Druckschrift)*:

Properties of dissipatively coupled optomechanical systems

Name, Vorname *(Druckschrift)*: Weiss, Talitha

Matrikelnummer: 07-054-364

Hiermit erkläre ich, dass mir bei der Abfassung dieser Arbeit nur die darin angegebene Hilfe zuteil wurde und dass ich sie nur mit den in der Arbeit angegebenen Hilfsmitteln verfasst habe.

Ich habe sämtliche verwendeten Quellen erwähnt und gemäss anerkannten wissenschaftlichen Regeln zitiert.

Diese Erklärung wird ergänzt durch eine separat abgeschlossene Vereinbarung bezüglich der Veröffentlichung oder öffentlichen Zugänglichkeit dieser Arbeit.

☐ ja ☒ nein

Ort, Datum: Basel, 7.12.12

Unterschrift: T. Weiß

Dieses Blatt ist in die Bachelor-, resp. Masterarbeit einzufügen.

Contents

Introduction

The field of *optomechanics* deals with systems in which optical and mechanical degrees of freedom are coupled to each other. Interaction between light and mechanical elements was already considered centuries ago by Johannes Kepler, who studied the tails of comets. Nowadays it is well known that light exerts a radiation pressure force on objects. The momentum of the impinging light is transferred to the mechanical object and thus influences its motion. Although the action of sunlight on comets looks spectacular and impressive, the force due to a single photon is small compared to the inertia of macroscopic objects. Nevertheless, radiation pressure has to be taken into account for precision measurements and is a major issue e.g. for the detection of gravitational waves. To make use of the radiation pressure force, it is convenient to use cavities to enhance the light intensity and thereby the coupling strength. A typical optomechanical setup consists of a cavity with one fixed and one moveable end-mirror, see Fig. 0.1 (a). The light circulating in the cavity displaces the moveable mirror and thus changes the cavity length. This, in turn, shifts the resonance frequency of the cavity, which influences the intensity and thereby the force on the mirror. In general, systems where the coupling between optical and mechanical degree of freedom arises due to a displacement-dependent cavity frequency are called *dispersively* coupled. The generic picture of a cavity with one moveable mirror captures the main idea of such setups, however many different experimental realizations exist, including e.g. cantilevers, membranes or microcavaties (see Fig. 0.2) with frequencies from Hz to GHz and masses from 10^{-20}g to kg [1].

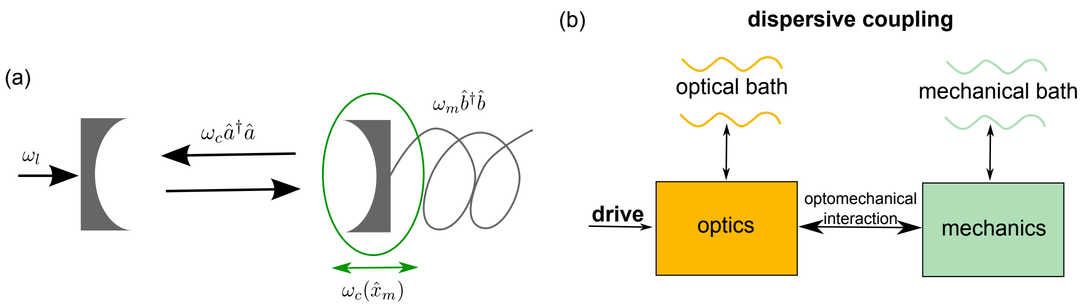

Figure 0.1.: (a) Typical optomechanical system implementing dispersive coupling between optics and mechanics. (b) Schematic picture illustrating the general setup envisioned for dispersively coupled systems, also including coupling to the environment.

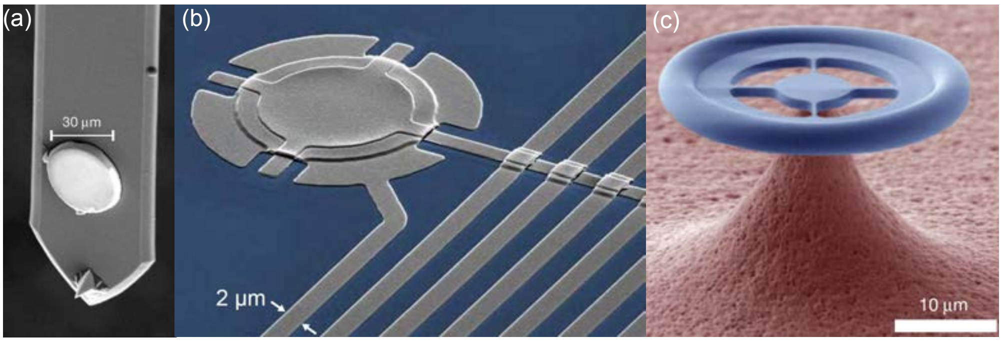

Figure 0.2.: (a) Cantilever tip with an attached mirror (picture taken from [2]). (b) Superconducting microwave resonator including a micromechanical membrane (picture taken from [3]). (c) Micro-toroidal resonator with an optical whispering-gallery mode and mechanical breathing modes (picture taken from [4]).

Interest in cavity optomechanical systems arises due to a wide range of possible applications in precision measurement, quantum information, and fundamental tests of quantum mechanics [1,5–7]. Cooling such optomechanical systems to their ground state is of importance, since it is a necessary condition for quantum state preparation. Driving a dispersively coupled systems at a frequency that is red-detuned from the cavity resonance can lead to cooling. This has been theoretically analyzed in Refs. [8, 9], and the quantum ground-state has now been reached in several experiments [3,10]. In the strong-coupling regime the optical and mechanical degrees of freedom hybridize. Normal-mode splitting has been predicted [11], and it was subsequently observed [12] in the optical output spectrum. If the system is probed with an additional probe field, the existence of the two normal modes can lead to destructive interference and a narrow transparency window at the cavity frequency [13]. For dispersive coupling this has been demonstrated experimentally [14, 15].

Figure 0.1 (b) illustrates the basic scheme of a dispersively-coupled optomechanical system: optics and mechanics interact directly and couple independently to separate baths. Recently, a different kind of optomechanics has been proposed [16]: a displacement-dependent cavity linewidth leads to a *dissipative coupling* between the mechanical and the optical degrees of freedom. This leads to a very different basic scheme, since the mechanics manipulates the coupling of the optics to the optical bath by influencing the cavity linewidth. Experimental realizations of this idea have been proposed in the microwave domain for superconducting resonators [16] and in the optical domain for a Michelson-Sagnac interferometer containing a moving membrane [17]. A first experiment that demonstrated dissipative coupling has been carried out with a microdisk resonator coupled to a nanomechanical waveguide [18]. It has been pointed out early on that dissipative coupling enables ground-state cooling outside the resolved-sideband limit and has potential applications in quantum-limited position measurements [16]. Moreover, squeezing of the mechanical state [19] and normal-mode splitting in response to a weak probe field [20] have been discussed in the context of the experimental setup of Ref. [18]. However, up to date, many properties of dissipatively coupled systems remain unknown.

In this Master Thesis we study the general case of an optomechanical system with dispersive as well as dissipative coupling. The first chapter introduces the theoretical model and gives a brief overview of proposed and realized experimental setups. In the second chapter, we focus on weak coupling and employ a quantum noise approach to calculate the force spectrum. From this we derive the optically-induced damping and frequency shift of the mechanical oscillator, known as backaction damping and optical spring effect. In contrast to dispersive coupling, we find that dissipatively coupled systems feature two parameter regions of amplification and two parameter regions of cooling. The third chapter deals with features arising if strong optomechanical coupling is applied and thus the exact solution to the linearized problem is used. We discuss the mechanical and optical spectra and especially focus on the signatures of normal-mode splitting. Moreover, cooling in the strong-coupling regime is briefly addressed using the covariance matrix formalism. In the fourth chapter we present optomechanical induced transparency as a convenient way to observe normal-mode splitting. Finally, we summarize our results and give an outlook on open questions concerning dissipatively coupled systems. Appendix A provides a list of variables and Appendix B some more detailed calculations.

Note, that the main results of this work have been published in "Strong-coupling effects in dissipatively coupled optomechanical systems", Talitha Weiss, Christoph Bruder, Andreas Nunnenkamp, *New Journal of Physics*, volume 15, 045017 (2013).

1. Dissipatively coupled optomechanical systems

This chapter introduces dissipatively coupled optomechanical systems. We present the theoretical description considering dispersive and dissipative coupling, such that the well-known results in the case of purely dispersive coupling are included as a special case of our more general approach. From the Hamiltonian we derive and linearize Heisenberg equations of motion which are the basis for most of the calculations done within this thesis. Finally, we give an overview of proposed and realized experimental setups and point out the differences to dispersively coupled systems.

1.1. Theoretical description

In this section we will provide the theoretical description used throughout this work to describe optomechanical systems including both dispersive and dissipative coupling. In Subsection 1.1.1 we introduce the Hamiltonian and derive Heisenberg equations of motion for the mechanical and optical mode. These equations of motion are linearized in Subsection 1.1.2 which also leads to a pair of classical equations.

1.1.1. Hamiltonian and equations of motion

We consider an optomechanical system consisting of a mechanical oscillator with resonance frequency ω_m and a cavity mode with resonance frequency ω_c. Dispersive coupling corresponds to a shift of the cavity resonance frequency due to the motion of the mechanical oscillator; dissipative coupling leads to a shift of the cavity damping rate κ due to the mechanical motion. Using an expansion to first order in the displacement $\hat{x}_m$ we find

$$\begin{aligned} \omega_c(\hat{x}_m) &\approx \omega_c(0) + \left(\frac{d\omega_c(x)}{dx}\right)\bigg|_{x=0} \hat{x}_m \\ \sqrt{\kappa(\hat{x}_m)} &\approx \sqrt{\kappa(0)} + \frac{1}{2}\frac{1}{\sqrt{\kappa(0)}}\left(\frac{d\kappa(x)}{dx}\right)\bigg|_{x=0} \hat{x}_m, \end{aligned} \tag{1.1}$$

where the dimensionless coupling strengths $\tilde{A}$ (dispersive) and $\tilde{B}$ (dissipative) are defined as $\tilde{A}\kappa = -\frac{d\omega_c(x)}{dx}x_0$ and $\tilde{B}\kappa = \frac{d\kappa(x)}{dx}x_0$, respectively. Here, $\omega_c \equiv \omega_c(0)$ and $\kappa \equiv \kappa(0)$ are the values of the uncoupled system at its equilibrium position. With $\hbar = 1$, the size of zero-point fluctuations is given by $x_0 = (2m\omega_m)^{-1/2}$, with m the mass of the mechanical oscillator. The Hamiltonian of the coupled system is given by [16]

$$
\begin{aligned}
\hat{\mathscr{H}} &= \omega_c(\hat{x}_m)\hat{a}^\dagger\hat{a} + \omega_m\hat{b}^\dagger\hat{b} + \sum_q \omega_q\hat{b}_q^\dagger\hat{b}_q - i\sqrt{\frac{\kappa(\hat{x}_m)}{2\pi\rho}}\sum_q\left(\hat{a}^\dagger\hat{b}_q - \hat{b}_q^\dagger\hat{a}\right) + \hat{H}_\gamma \\
&= \omega_c\hat{a}^\dagger\hat{a} + \omega_m\hat{b}^\dagger\hat{b} - \left[\tilde{A}\kappa\hat{a}^\dagger\hat{a} + i\sqrt{\frac{\kappa}{2\pi\rho}}\frac{\tilde{B}}{2}\sum_q\left(\hat{a}^\dagger\hat{b}_q - \hat{b}_q^\dagger\hat{a}\right)\right]\frac{\hat{x}_m}{x_0} + \hat{H}_\kappa + \hat{H}_\gamma.
\end{aligned}
\tag{1.2}
$$

Regarding the second equality sign, the first term describes the cavity mode, where $\hat{a}^\dagger$ ($\hat{a}$) are bosonic creation (annihilation) operators. The second term describes the mechanical oscillator, where $\hat{b}^\dagger$ ($\hat{b}$) are bosonic creation (annihilation) operators. The cavity has a linewidth κ, and the mechanical oscillator is damped at a rate γ. The damping due to the optical and mechanical bath is described by $\hat{H}_\kappa$ and $\hat{H}_\gamma$, respectively. The third term describes the optomechanical interaction, taking into account both dispersive and dissipative coupling. Here, $\hat{b}_q^\dagger$ ($\hat{b}_q$) are bosonic creation (annihilation) operators describing the optical bath coupled to the cavity, ω_q is the frequency of the bath mode q, and ρ denotes the density of states of the optical bath, treated as a constant for the relevant frequencies. $\tilde{B} = 0$ corresponds to the well-investigated case of purely dispersive coupling and $\tilde{A} = 0$ to the case of purely dissipative coupling.

To derive the Heisenberg equations of motion, we adapt the input-output formalism [21] to dissipative coupling, see Appendix B.1. This leads to the following expression

$$
\sqrt{\frac{\kappa}{2\pi\rho}}\sum_q\hat{b}_q = \sqrt{\kappa}\hat{a}_{\text{in}} + \frac{\kappa}{2}\hat{a} + \frac{\kappa}{2}\frac{\tilde{B}}{2}\frac{\hat{x}_m}{x_0}\hat{a},
\tag{1.3}
$$

where $\hat{a}_{\text{in}}$ is the optical input mode [22]. The new input-output relation is given by [17]

$$
\hat{a}_{\text{in}} - \hat{a}_{\text{out}} = -\sqrt{\kappa}\hat{a} - \frac{\sqrt{\kappa}\tilde{B}}{2x_0}\hat{x}_m\hat{a}.
\tag{1.4}
$$

Note that the last term only contributes for nonzero dissipative coupling and introduces an explicit $\hat{x}_m$-dependence as well as a nonlinearity into the input-output relation.

Using Eq. (1.3), the Heisenberg equations of motion for the mechanical and the cavity mode are

$$
\dot{\hat{b}} = -\left(i\omega_m + \frac{\gamma}{2}\right)\hat{b} - \sqrt{\gamma}\hat{\eta} + i\tilde{A}\hat{a}^\dagger\hat{a} - \frac{\tilde{B}}{2}\sqrt{\kappa}\left(\hat{a}^\dagger\hat{a}_{\text{in}} - \hat{a}_{\text{in}}^\dagger\hat{a}\right)
\tag{1.5}
$$

$$
\dot{\hat{a}} = -i\left(\omega_c - \tilde{A}\kappa\frac{\hat{x}_m}{x_0}\right)\hat{a} - \left(1 + \frac{\tilde{B}}{2}\frac{\hat{x}_m}{x_0}\right)\sqrt{\kappa}\hat{a}_{\text{in}} - \left[1 + \tilde{B}\frac{\hat{x}_m}{x_0} + \left(\frac{\tilde{B}}{2}\right)^2\frac{\hat{x}_m^2}{x_0^2}\right]\frac{\kappa}{2}\hat{a}.
\tag{1.6}
$$

However, it is not justified to keep the term proportional to $\hat{x}_m^2$ in Eq. (1.6), since in Eq. (1.1) only terms up to first order in $\hat{x}_m$ were considered. Treating everything up to second order in $\hat{x}_m$, it turns out that this term indeed drops out, see Appendix B.2.

Thus, the equations of motion correct up to first order in $\hat{x}_m$ are

$$\dot{\hat{b}} = -\left(i\omega_m + \frac{\gamma}{2}\right)\hat{b} - \sqrt{\gamma}\hat{\eta} + i\tilde{A}\hat{a}^\dagger\hat{a} - \frac{\tilde{B}}{2}\sqrt{\kappa}\left(\hat{a}^\dagger\hat{a}_{\text{in}} - \hat{a}_{\text{in}}^\dagger\hat{a}\right) \tag{1.7}$$

$$\dot{\hat{a}} = -i\left(\omega_c - \tilde{A}\kappa\frac{\hat{x}_m}{x_0}\right)\hat{a} - \left(1 + \frac{\tilde{B}}{2}\frac{\hat{x}_m}{x_0}\right)\sqrt{\kappa}\hat{a}_{\text{in}} - \left(1 + \tilde{B}\frac{\hat{x}_m}{x_0}\right)\frac{\kappa}{2}\hat{a}. \tag{1.8}$$

1.1.2. Linearization

In the following, we consider a strong, coherent optical drive and linearize Eqs. (1.7) and (1.8). Using $\hat{a} = (\bar{a} + \hat{d})e^{-i\omega_d t}$, $\hat{b} = \bar{b} + \hat{c}$, $\hat{a}_{\text{in}} = (\bar{a}_{\text{in}} + \hat{\xi}_{\text{in}})e^{-i\omega_d t}$, and Eq. (1.3), we obtain the linearized equations of motion in a frame rotating at the drive frequency ω_d

$$\dot{\hat{c}} = -\left(i\omega_m + \frac{\gamma}{2}\right)\hat{c} - \sqrt{\gamma}\hat{\eta} + i\tilde{A}\kappa\left(\bar{a}^*\hat{d} + \bar{a}\hat{d}^\dagger\right) - \frac{\tilde{B}}{2}\sqrt{\kappa}\left(\bar{a}^*\hat{\xi}_{\text{in}} - \bar{a}\hat{\xi}_{\text{in}}^\dagger\right) - i\frac{\tilde{B}}{2}\left(\Omega^*\hat{d} + \Omega\hat{d}^\dagger\right), \tag{1.9}$$

$$\dot{\hat{d}} = i\left(\Delta + \tilde{A}\kappa\frac{\bar{x}}{x_0}\right)\hat{d} - \frac{\kappa}{2}\left(1 + \tilde{B}\frac{\bar{x}}{x_0}\right)\hat{d} - \sqrt{\kappa}\left(1 + \frac{\tilde{B}}{2}\frac{\bar{x}}{x_0}\right)\hat{\xi}_{\text{in}} + \left(i\tilde{A}\kappa\bar{a} - \frac{\kappa}{2}\tilde{B}\bar{a} - i\Omega\frac{\tilde{B}}{2}\right)\frac{\hat{x}}{x_0}. \tag{1.10}$$

In this expression, $\Delta = \omega_d - \omega_c$ is the detuning between drive and cavity frequency, $\Omega = -i\sqrt{\kappa}\bar{a}_{\text{in}}$ is the strength of the coherent laser drive, and $\hat{x} = x_0(\hat{c}^\dagger + \hat{c})$ is the displacement of the mechanical oscillator relative to its steady-state position $\bar{x}$, i.e. $\hat{x}_m = \bar{x} + \hat{x}$. The thermal noise influencing the mechanical oscillator is described by the noise operators $\hat{\eta}$ and $\hat{\eta}^\dagger$. The bath coupled to the mechanical oscillator is assumed to be Markovian and at a temperature T associated with an equilibrium phonon number $n_{\text{th}} = [\exp(\omega_m/k_B T) - 1]^{-1}$, i.e. $\langle\hat{\eta}^\dagger(\omega)\hat{\eta}(\omega')\rangle = 2\pi\delta(\omega+\omega')n_{\text{th}}$ and $\langle\hat{\eta}(\omega)\hat{\eta}^\dagger(\omega')\rangle = 2\pi\delta(\omega+\omega')(n_{\text{th}}+1)$ where k_B denotes Boltzmann's constant. The operators $\hat{\xi}_{\text{in}}$ and $\hat{\xi}_{\text{in}}^\dagger$ describe the noise induced by the optical bath which is assumed to be vacuum noise, i.e. $\langle\hat{\xi}_{\text{in}}(\omega)\hat{\xi}_{\text{in}}^\dagger(\omega')\rangle = 2\pi\delta(\omega+\omega')$.

From Eq. (1.9) it is apparent that dissipative coupling $\tilde{B}$ has a twofold influence on the motion of the mechanical oscillator: There is a cavity-mediated influence which is very similar to the dispersive coupling term, except for the amplification by the drive strength Ω instead of the cavity amplitude $\bar{a}$. In addition, dissipative coupling leads to a direct influence of the optical bath on the mechanics.

In Eq. (1.10), dissipative coupling leads to a change in the damping rate κ, whereas dispersive coupling $\tilde{A}$ leads to a change in the detuning Δ. These shifts can be determined from the steady-state solutions of the classical equations of motion

$$0 = \dot{\bar{b}} = -\left(i\omega_m + \frac{\gamma}{2}\right)\bar{b} + i\tilde{A}\kappa\left|\bar{a}\right|^2 - i\frac{\tilde{B}}{2}\left(\Omega\bar{a}^* + \Omega^*\bar{a}\right) \tag{1.11}$$

$$0 = \dot{\bar{a}} = i\left(\Delta + \tilde{A}\kappa\frac{\bar{x}}{x_0}\right)\bar{a} - \left(1 + \frac{\tilde{B}}{2}\frac{\bar{x}}{x_0}\right)i\Omega - \left(1 + \tilde{B}\frac{\bar{x}}{x_0}\right)\frac{\kappa}{2}\bar{a}, \tag{1.12}$$

where $\bar{x} = x_0(\bar{b} + \bar{b}^*)$. These equations give rise to a static bistability, even if purely dissipative coupling, i.e. $\tilde{A} = 0$, is considered. A brief discussion of the classical equations can be found in Appendix B.3. However, to proceed we focus on parameters leading to a unique solution and for which the shifts due to $\bar{x}$ are sufficiently small. In this case we use the steady-state solution of the uncoupled system, i.e. $\tilde{A} = \tilde{B} = 0$, and Eqs. (1.11) and (1.12) simplify to

$$0 = -\left(i\omega_m + \frac{\gamma}{2}\right)\bar{b} \tag{1.13}$$

$$0 = i\Delta\bar{a} - i\Omega - \frac{\kappa}{2}\bar{a}, \tag{1.14}$$

with solutions $\bar{b} = 0$, implying $\bar{x} = 0$, and $i\Omega = (i\Delta - \kappa/2)\bar{a}$, providing a relation between the intra-cavity amplitude $\bar{a}$ and the drive strength Ω. Throughout this work we will fix $\bar{a}$, hence the drive strength will vary depending on the detuning. Substituting the steady-state results into Eqs. (1.9) and (1.10) we end up with

$$\dot{\hat{c}} = -\left(i\omega_m + \frac{\gamma}{2}\right)\hat{c} - \sqrt{\gamma}\hat{\eta} + i\tilde{A}\kappa\left(\bar{a}^*\hat{d} + \bar{a}\hat{d}^\dagger\right) - \frac{\tilde{B}}{2}\sqrt{\kappa}\left(\bar{a}^*\hat{\xi}_{\mathrm{in}} - \bar{a}\hat{\xi}_{\mathrm{in}}^\dagger\right) - \frac{\tilde{B}}{2}\left[\left(i\Delta + \frac{\kappa}{2}\right)\bar{a}^*\hat{d} + \left(i\Delta - \frac{\kappa}{2}\right)\bar{a}\hat{d}^\dagger\right] \tag{1.15}$$

$$\dot{\hat{d}} = i\Delta\hat{d} - \frac{\kappa}{2}\hat{d} - \sqrt{\kappa}\hat{\xi}_{\mathrm{in}} + \left[i\tilde{A}\kappa\bar{a} - \frac{\kappa}{2}\tilde{B}\bar{a} - \left(i\Delta - \frac{\kappa}{2}\right)\bar{a}\frac{\tilde{B}}{2}\right]\frac{\hat{x}}{x_0}. \tag{1.16}$$

1.2. Experimental setups

In this section we want to give a brief overview of proposed and realized setups for dissipative coupling. Figure 1.1 (b) shows the schematic circuit diagram of an implementation in the microwave domain for superconducting resonators [16]. For comparison, Fig. 1.1 (a) illustrates the schematic circuit diagram that implements a purely dispersively coupled system. In both cases a LC-resonator plays the role of a cavity and an input capacitor C_1 determines the coupling to the drive from a feed line. This driving port is also assumed to be the port through which fluctuations enter the system, i.e. it plays the role of the optical bath. In the case of purely dispersive coupling the displacement-dependent capacitor $C_0(x)$ modulates the resonance frequency of the LC resonator, whereas the coupling to the feed line is constant. Thus, the interaction of the optical bath and drive with the mechanical oscillator is completely mediated by the cavity, cf. Fig. 0.1 (b). In contrast, a displacement-dependent input capacitor $C_1(x)$ leads to dissipative coupling, since it modulates the effective drive strength and damping rate. Dissipative coupling also leads to a cavity-mediated influence on the mechanics, but in contrast to dispersive coupling it is proportional to the drive strength Ω and not to the intra-cavity amplitude $\bar{a}$ (cf. Eq. (1.9)). In addition, for dissipative coupling the mechanical displacement enters directly in the coupling to the optical bath and thus the mechanical oscillator is also directly influenced by the optical bath. This will lead to several new features in dissipatively coupled systems.

In addition to this electromechanical setup, there is a recent proposal in the optical domain to use a Michelson-Sagnac interferometer [17]. A moveable membrane is po-

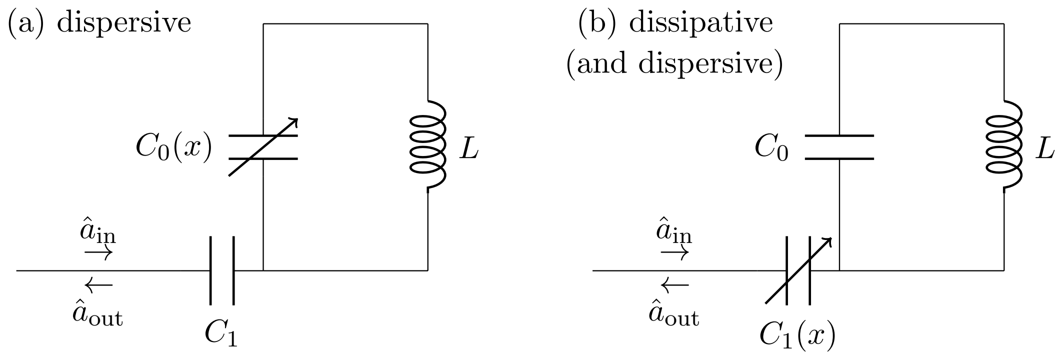

Figure 1.1.: (a) Electromechanical implementation of a dispersively coupled system ($\tilde{B} = 0$). The resonance frequency of the LC resonator depends on the displacement-dependent capacitance $C_0(x)$. The static input capacitor C_1 determines the coupling strength between resonator and feed line. (b) Electromechanical implementation of a dissipatively coupled system [16]. Compared to (a) only the role of the capacitors is interchanged. This leads to a displacement-dependent coupling of the circuit to the feed line. As the total capacitance and thus the resonance frequency is displacement-dependent, the dispersive coupling is nonzero also in this case (i.e. $\tilde{A} \neq 0$ and $\tilde{B} \neq 0$).

sitioned inside the interferometer and the complete configuration behaves like a cavity with an effective, moveable mirror, see Fig. 1.2 A. Advantageously, such a setup allows to tune the ratio of dispersive and dissipative coupling, i.e. $\tilde{A}/\tilde{B}$, and realize e.g. purely dissipative coupling.

A first experimental demonstration of dissipative coupling was achieved with a microdisk coupled to a vibrating nanomechanical waveguide, see Fig. 1.2 B [18]. The investigated device leads to dispersive and dissipative coupling, but with a dominating dissipative coupling strength. It was demonstrated that dissipative coupling gives rise to an optical force that can be either attractive or repulsive, depending on the detuning.

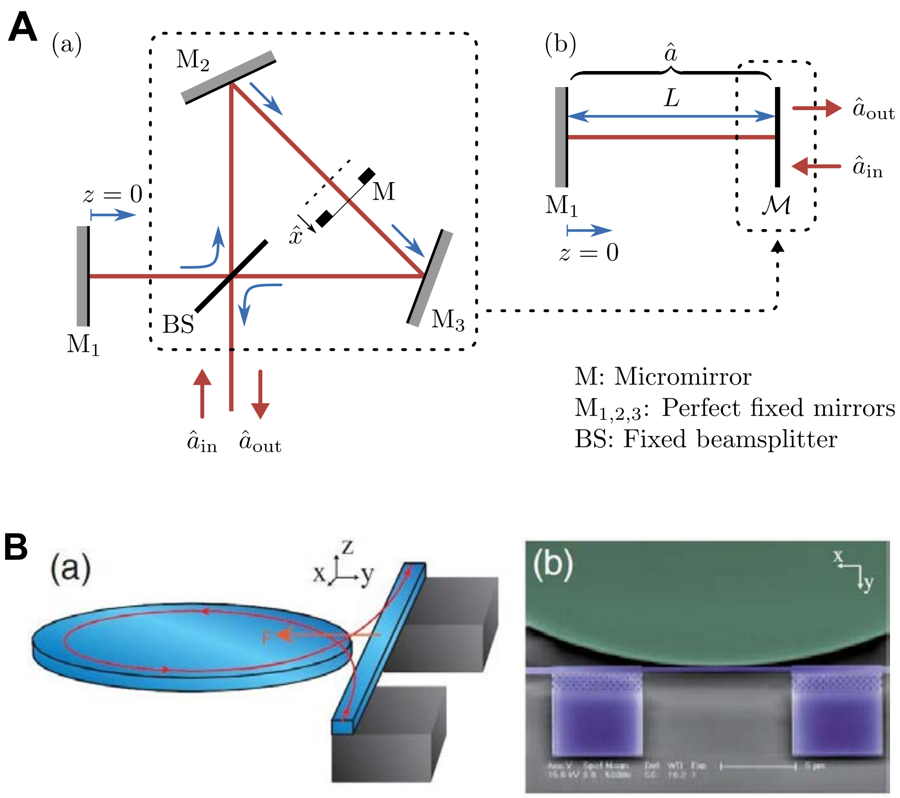

Figure 1.2.: **A** Proposed setup of a Michelson-Sagnac interferometer with a moveable membrane M (a). The complete configuration behaves like a cavity with an effective, moveable mirror $\mathcal{M}$ (b) (picture taken from Ref. [17]). **B** Nanomechanical waveguide coupled to a microdisk, (a) schematic diagram, (b) scanning electron microscopy image of the device (picture taken from Ref. [18]).

2. Quantum noise approach

Although the linearized equations of motion can be solved exactly, see Sec. 3.1, additional physical insight can be gained using a weak-coupling approach. The basic idea is to treat the influences of the optomechanical coupling on the mechanical oscillator as additional quantum noise sources. Most of the relevant properties are then connected to the weak-coupling force spectrum, which is modified in the case of dissipative coupling compared to purely dispersive coupling. In particular, we discuss optically-induced damping, the optical spring effect and cooling of the mechanical motion, and compare the results for different types of coupling.

2.1. The weak-coupling force spectrum

For sufficiently small coupling strengths the effects of the optomechanical coupling on the mechanical oscillator, i.e. the influence of the force $\hat{F}$ associated with the interaction term in Eq. (1.2), can be treated as a quantum noise source. This allows to derive transition rates between neighbouring phonon number states, $\Gamma_{n\to n+1}$ and $\Gamma_{n\to n-1}$, given by Fermi's Golden Rule. Defining an amplification rate $\Gamma_\uparrow = \Gamma_{n\to n+1}/(n+1) = x_0^2 S_{FF}(-\omega_m)$ as well as a cooling rate $\Gamma_\downarrow = \Gamma_{n\to n-1}/n = x_0^2 S_{FF}(\omega_m)$ independent of the phonon number, both $\Gamma_\uparrow$ and $\Gamma_\downarrow$ are determined by the weak-coupling force spectrum $S_{FF}(\omega)$ [22, 23]. To calculate $S_{FF}(\omega) = \int_{-\infty}^{+\infty} d\omega' \langle \hat{F}(\omega)\hat{F}(\omega')\rangle/2\pi$ we use the backaction force operator [16]

$$\hat{F}x_0 = \tilde{A}\kappa(\bar{a}^*\hat{d} + \bar{a}\hat{d}^\dagger) + i\frac{\tilde{B}}{2}\sqrt{\kappa}(\bar{a}^*\hat{\xi}_{\text{in}} - \bar{a}\hat{\xi}_{\text{in}}^\dagger) - \frac{\tilde{B}}{2}(\Omega^*\hat{d} + \Omega\hat{d}^\dagger) \tag{2.1}$$

which can be determined from the interaction part of the Hamiltonian, i.e. the third term of Eq. (1.2), using Eq. (1.3) in a linearized form. Since we assume weak coupling, it is sufficient to take the influence of the original cavity field into account, i.e. we neglect the modifications of $\hat{d}$ due to the optomechanical coupling. Thus, we solve Eq. (1.16) in absence of coupling, $\tilde{A} = \tilde{B} = 0$. In Fourier space, this leads to $\hat{d}(\omega) = -\sqrt{\kappa}\chi_c(\omega)\hat{\xi}_{\text{in}}(\omega)$, where $\chi_c(\omega) = [\kappa/2 - i(\omega + \Delta)]^{-1}$ denotes the cavity response function. Note that the Fourier transformation is applied such that $\hat{Q}^\dagger(\omega) = [\hat{Q}(-\omega)]^\dagger$ for all operators, thus $\hat{d}^\dagger(\omega) = -\sqrt{\kappa}\chi_c(-\omega)\hat{\xi}_{\text{in}}^\dagger(\omega)$. Substituting this solutions for $\hat{d}$ and $\hat{d}^\dagger$, and the relation $\Omega = -i\bar{a}(i\Delta - \kappa/2)$ into Eq. (2.1), the force operator becomes

$$\hat{F}x_0 = \sqrt{\kappa}\left[-\tilde{A}\kappa\bar{a}^*\chi_c(\omega) + i\frac{\tilde{B}}{2}\bar{a}^* + i\frac{\tilde{B}}{2}\bar{a}^*\left(-i\Delta - \frac{\kappa}{2}\right)\chi_c(\omega)\right]\hat{\xi}_{\text{in}}(\omega) + \text{H.c.}. \tag{2.2}$$

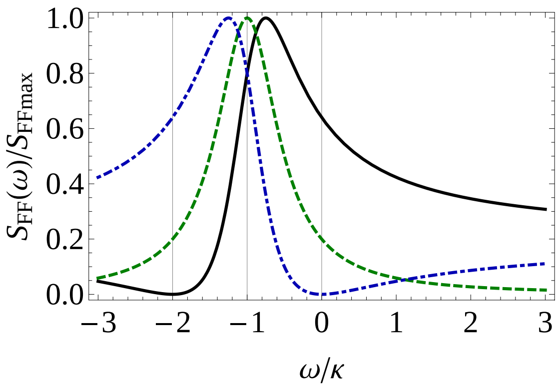

Figure 2.1.: Weak-coupling force spectrum $S_{FF}(\omega)$ in the case of purely dissipative coupling (black solid line), purely dispersive coupling (green dashed line) and for mixed coupling $\tilde{A}/\tilde{B} = 1$ (blue dot-dashed line) at detuning $\Delta = \kappa$. The grid lines indicate the maximum of the green dashed Lorentzian and the zeros of the black solid and blue dot-dashed Fano line shape, respectively.

The weak-coupling force spectrum can be calculated using $\langle \hat{\xi}_{\rm in}(\omega)\hat{\xi}^\dagger_{\rm in}(\omega')\rangle = 2\pi\delta(\omega+\omega')$ and $\langle \hat{\xi}^\dagger_{\rm in}(\omega)\hat{\xi}_{\rm in}(\omega')\rangle = 0$, and is given by [16]

$$\begin{aligned} S_{FF}(\omega) &= \int_{-\infty}^{+\infty} \frac{d\omega'}{2\pi} \langle \hat{F}(\omega)\hat{F}(\omega')\rangle \\ &= \kappa \left(\frac{\tilde{B}|\bar{a}|}{2x_0}\right)^2 \left| 1 + \left(-i\Delta - \frac{\kappa}{2} + i\frac{2\tilde{A}\kappa}{\tilde{B}}\right)\chi_c(\omega)\right|^2 \\ &= \kappa \left(\frac{\tilde{B}|\bar{a}|}{2x_0}\right)^2 |\chi_c(\omega)|^2 \left(\omega + 2\Delta - \frac{2\tilde{A}\kappa}{\tilde{B}}\right)^2 . \end{aligned} \tag{2.3}$$

In the general case of dispersive and dissipative coupling (or purely dissipative coupling) the result is a Fano line shape which reduces to a Lorentzian in absence of dissipative coupling, i.e. $\tilde{B} = 0$. As discussed in Ref. [16] the Fano line shape originates from an interference effect between the two ways of interaction with the mechanics. These two processes act as two noise sources influencing the mechanical oscillator, and lead to the two terms inside the absolute value in Eq. (2.3): The constant first term accounts for the direct interaction between optical bath and mechanical oscillator and represents coupling to a continuum. In contrast, the second term is filtered by the cavity response $\chi_c(\omega)$ and arises due to the influence of the cavity. The interference of these two contributions, the direct action of the optical bath and its cavity-mediated influence, gives rise to the Fano line shape. Purely dispersive coupling leads only to a filtered, cavity-mediated influence, i.e. the mechanical oscillator is only affected by a single optical noise source, and no interference can occur.

Figure 2.1 shows the force spectrum for purely dispersive, purely dissipative and equally mixed coupling. Notably, the Fano line shape has an exact zero whereas the Lorentzian has none. This zero can directly be read off the last equality of Eq. (2.3) and leads to a relation between the detuning Δ and the frequency ω, i.e.

$$\Delta_0(\omega) = -\omega/2 + \kappa\tilde{A}/\tilde{B} \tag{2.4}$$

determines the detuning for which $S_{FF}(\omega) = 0$. The importance of this feature of the Fano line shape is due to the existence of an optimal detuning [16]

$$\Delta_{\text{opt}} \equiv \Delta_0(-\omega_m) = \omega_m/2 + \kappa\tilde{A}/\tilde{B}, \tag{2.5}$$

which implies $S_{FF}(-\omega_m) = 0$ and $\Gamma_\uparrow = 0$. The implications of this for cooling will be discussed in Section 2.3.

2.2. Optical damping and optically-induced frequency shift

In absence of optomechanical coupling the mechanical oscillator is coupled to the mechanical bath only. Thus the oscillator is damped at a rate γ which leads to a mean phonon number in thermal equilibrium, n_{th}. Together with the resonance frequency ω_m, these quantities determine the mechanical spectrum $S_{cc}(\omega)$ which is a Lorentzian of width γ (FWHM) with a peak at $-\omega_m$ and an area of $2\pi n_{\text{th}}$.

The cooling and amplification rates $\Gamma_\downarrow$ and $\Gamma_\uparrow$, defined in the last section, lead to an optically-induced damping $\gamma_{\text{opt}} = \Gamma_\downarrow - \Gamma_\uparrow = x_0^2[S_{FF}(\omega_m) - S_{FF}(-\omega_m)]$ and a minimal phonon number $n_{\text{opt}} = \Gamma_\uparrow/x_0^2\gamma_{\text{opt}} = S_{FF}(-\omega_m)/\gamma_{\text{opt}}$ [22,23]. In the presence of both the mechanical bath and the optomechanical coupling, this results in a total damping $\gamma_{\text{tot}} = \gamma + \gamma_{\text{opt}}$ which determines the new width of the Lorentzian describing the mechanical spectrum $S_{cc}(\omega)$. Furthermore, the additional damping leads to a steady-state mean phonon number $n_{\text{osc}} = (\gamma n_{\text{th}} + \gamma_{\text{opt}} n_{\text{opt}})/(\gamma_{\text{opt}} + \gamma)$, thus the area of the Lorentzian is changed. Finally, optical damping affects the effective spring constant, corresponding to a shift of the mechanical frequency given by $\delta\omega_m = \int d\omega S_{FF}(\omega)[1/(\omega_m - \omega) - 1/(\omega_m + \omega)]/2\pi$ [8], see Appendix B.4 for a detailed derivation. In summary, the modifications of the mechanical spectrum $S_{cc}(\omega)$ due to weak optomechanical coupling can be described by the parameters γ_{opt}, n_{osc} and $\delta\omega_m$.

So far our considerations do not explicitly depend on the type of the coupling. However, the force spectrum $S_{FF}(\omega)$ contains this information, i.e. its shape depends on the applied coupling. Figure 2.2 (a) shows the optical damping for purely dispersive and purely dissipative coupling. Since $\tilde{B} = 0$ means that the force spectrum is a Lorentzian, the optical damping γ_{opt} is given by the difference of two Lorentzians. Choosing $\Delta \approx -\omega_m$ maximizes the optical damping rate. In contrast, since the force spectrum $S_{FF}(\omega)$ is a Fano line shape for dissipative coupling (purely or in addition to dispersive coupling), the optical damping rate is modified [16]. The maximum is shifted farther away from the mechanical resonance frequency ω_m and for $|\Delta| \gg \kappa$ the optical damping rate decreases more slowly than a Lorentzian and is proportional $-1/\Delta$.

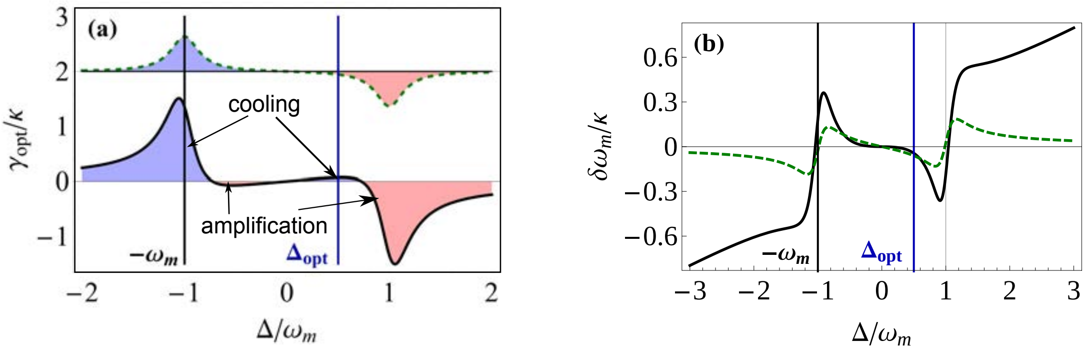

Figure 2.2.: Optical damping γ_{opt} (a) and optically-induced frequency shift $\delta\omega_m$ (b) as a function of detuning Δ. The dashed, green lines show the result for purely dispersive coupling ($\tilde{A}\bar{a} = 0.4, \tilde{B} = 0$), the solid, black lines show purely dissipative coupling ($\tilde{A} = 0, \tilde{B}\bar{a} = 0.4$). Blue (red) areas in (a) indicate cooling (amplification). The sideband parameter is $\omega_m/\kappa = 3$.

Furthermore, for typical parameters we find two regions where the optical damping is positive, thus providing cooling, as well as two regions with negative γ_{opt}, leading to instability if $\gamma_{\mathrm{tot}} = \gamma + \gamma_{\mathrm{opt}} < 0$.

Figure 2.2 (b) shows the optically-induced frequency shift $\delta\omega_m$ for purely dispersive and purely dissipative coupling. Dispersive coupling and cooling at $\Delta = -\omega_m$ allows for a vanishing frequency shift $\delta\omega_m = 0$. In contrast, dissipative coupling leads to a nonzero frequency shift $\delta\omega_m$ at $\Delta = -\omega_m$. It remains small for small detunings only, for large values of Δ it increases linearly. Note that this linear dependence is due to the fact that we fix the number of photons inside the cavity $|\bar{a}|^2$, which implies that the drive strength Ω has to increase with the detuning Δ. Since dissipative coupling has a component proportional to Ω, the effective dissipative coupling strength is increased. Fixing the laser power instead, the intra-cavity amplitude $\bar{a}$ decreases as $1/\Delta$ and $\delta\omega_m \approx (\tilde{B}|\bar{a}|)^2\Delta/2$ goes to zero in the limit of large detunings $|\Delta| \gg \omega_m$.

2.3. Cooling in the weak-coupling limit

One possible choice to achieve cooling with dissipative coupling is $\Delta \approx -\omega_m$. Figure 2.3 shows that, for both purely dispersive and purely dissipative coupling, $\Delta \approx -\omega_m$ leads to a strong decrease of the phonon number n_{osc}. This is not surprising since the optical damping γ_{opt} is maximized close to this detuning in both cases. However, large optical damping alone is not sufficient to achieve the best cooling results in the sense of smallest n_{osc}. Notably, dispersive coupling at this detuning leads to smaller n_{osc} despite the larger optical damping rate of dissipative coupling, except for very small coupling strengths. This is due to a larger n_{opt} which also contributes to the mean phonon number n_{osc}. Thus it is of particular interest to achieve n_{opt} as small as possible. For dispersive coupling this

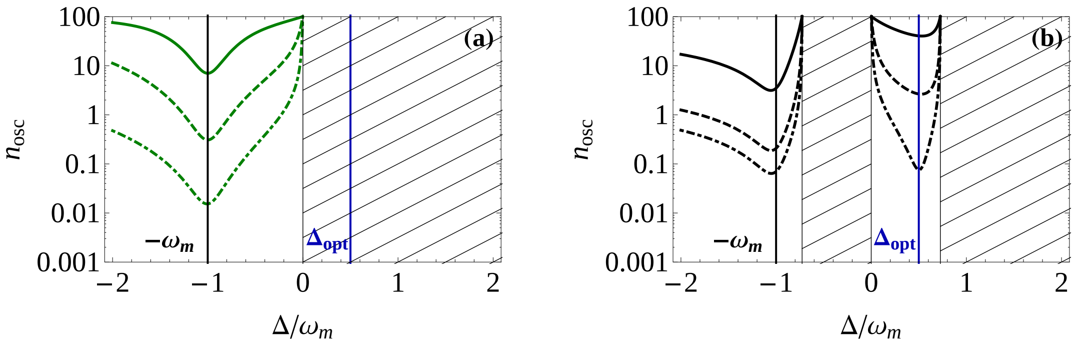

Figure 2.3.: Mean phonon number n_{osc} as a function of detuning Δ in the case of (a) purely dispersive coupling and (b) purely dissipative coupling. The solid lines show the result for (a) $\tilde{A}\bar{a} = 0.01$ and (b) $\tilde{B}\bar{a} = 0.01$, respectively, the dashed lines show (a) $\tilde{A}\bar{a} = 0.05$ and (b) $\tilde{B}\bar{a} = 0.05$, and the dot-dashed lines show (a) $\tilde{A}\bar{a} = 0.3$ and (b) $\tilde{B}\bar{a} = 0.3$. Other parameters are $\omega_m/\kappa = 3$, $\omega_m/\gamma = 10^5$, and $n_{\text{th}} = 100$. Hatched areas indicate unstable regions due to the criterion $\gamma_{\text{tot}} < 0$.

is linked to reaching the resolved-sideband limit [8]. In presence of dissipative coupling the zero of the Fano line shape of $S_{FF}(\omega)$, discussed in Section 2.1, leads to the optimal detuning Eq. (2.5) where $\Gamma_\uparrow = 0$ and thus $n_{\text{opt}} = 0$ [16]. Therefore the optomechanical coupling induces a cooling rate $\Gamma_\downarrow$ but no amplification rate $\Gamma_\uparrow$ and ground-state cooling can be achieved if the drive strength is sufficiently large or the intrinsic damping γ small enough. Fortunately these conditions are independent of the sideband parameter ω_m/κ and ground-state cooling can be performed in the unresolved-sideband regime that is easier to reach experimentally. Finally, since the optimal detuning is part of the second cooling region, $\Delta = \Delta_{\text{opt}}$ is far from maximizing the optical damping rate, see Fig. 2.2 (a). Compared to the values of γ_{opt} achieved at $\Delta = -\omega_m$ for either dispersive or dissipative coupling, the optical damping rate at $\Delta = \Delta_{\text{opt}}$ is rather small. Therefore, to achieve considerable cooling despite the poor cooling rate, stronger coupling or smaller intrinsic mechanical damping γ is required.

Note that in the case of purely dissipative coupling, i.e. $\tilde{A} = 0$, the optimal detuning $\Delta_{\text{opt}} = \omega_m/2$ corresponds to a blue detuned drive laser. On the contrary, driving a dispersively coupled system ($\tilde{B} = 0$) with this detuning would lead to amplification rather than cooling.

3. Strong coupling

In this chapter we want to investigate the influence of dissipative coupling on the mechanical and optical spectra beyond weak coupling. These spectra have the form $S_{kq}(\omega) = \int dt \langle \hat{k}^\dagger(t)\hat{q}(0)\rangle e^{i\omega t} = \int d\omega' \langle \hat{k}^\dagger(\omega)\hat{q}(\omega')\rangle/2\pi$ and, in our case, require the solutions of Eqs. (1.15) and (1.16). Thus, in Section 3.1, we solve the linearized equations of motion (1.15) and (1.16) exactly for the general case, including both dispersive and dissipative coupling. The stability of this solution is numerically checked for the set of parameters used throughout this work. Then, using the exact solution, we determine the trum in Section 3.2 and discuss its main features. We find normal-mode splitting and a striking feature that can be traced back to the Fano line shape in the weak-coupling force spectrum. Section 3.3 treats the optical spectra, i.e. the cavity and the optical output spectrum which inherit features from the mechanical spectrum due to the optomechanical coupling. We discuss the differences between the spectra of purely dispersively coupled and purely dissipatively coupled systems. Finally, in Section 3.4 we briefly comment on cooling in the strong-coupling regime and derive the mean phonon number using the covariance matrix formalism.

3.1. Exact solution of the linearized equations of motion

To solve the linearized equations of motion (1.15) and (1.16) it is convenient to transform them into Fourier space. Furthermore, due to their dependence on the hermitian conjugates $\hat{c}^\dagger$ and $\hat{d}^\dagger$ it is advantageous to proceed with the matrix equations

$$
\begin{aligned}
-i\omega \begin{pmatrix} \hat{d} \\ \hat{d}^\dagger \end{pmatrix} &= \begin{pmatrix} i\Delta - \kappa/2 & \\ & -i\Delta - \kappa/2 \end{pmatrix} \begin{pmatrix} \hat{d} \\ \hat{d}^\dagger \end{pmatrix} - \sqrt{\kappa} \begin{pmatrix} \hat{\xi}_{\text{in}} \\ \hat{\xi}_{\text{in}}^\dagger \end{pmatrix} \\
&+ \begin{pmatrix} -\frac{\tilde{B}}{2}\left[\kappa\bar{a} + (i\Delta - \kappa/2)\bar{a}\right] + i\tilde{A}\kappa\bar{a} & -\frac{\tilde{B}}{2}\left[\kappa\bar{a} + (i\Delta - \kappa/2)\bar{a}\right] + i\tilde{A}\kappa\bar{a} \\ -\frac{\tilde{B}}{2}\left[\kappa\bar{a}^* - (i\Delta + \kappa/2)\bar{a}^*\right] - i\tilde{A}\kappa\bar{a}^* & -\frac{\tilde{B}}{2}\left[\kappa\bar{a}^* - (i\Delta + \kappa/2)\bar{a}^*\right] - i\tilde{A}\kappa\bar{a}^* \end{pmatrix} \begin{pmatrix} \hat{c} \\ \hat{c}^\dagger \end{pmatrix}
\end{aligned} \tag{3.1}
$$

and

$$
\begin{aligned}
-i\omega \begin{pmatrix} \hat{c} \\ \hat{c}^\dagger \end{pmatrix} &= \begin{pmatrix} -i\omega_m - \gamma/2 & \\ & i\omega_m - \gamma/2 \end{pmatrix} \begin{pmatrix} \hat{c} \\ \hat{c}^\dagger \end{pmatrix} - \sqrt{\gamma} \begin{pmatrix} \hat{\eta} \\ \hat{\eta}^\dagger \end{pmatrix} + \begin{pmatrix} -\frac{\tilde{B}}{2}\sqrt{\kappa}\bar{a}^* & \frac{\tilde{B}}{2}\sqrt{\kappa}\bar{a} \\ \frac{\tilde{B}}{2}\sqrt{\kappa}\bar{a}^* & -\frac{\tilde{B}}{2}\sqrt{\kappa}\bar{a} \end{pmatrix} \begin{pmatrix} \hat{\xi}_{\text{in}} \\ \hat{\xi}_{\text{in}}^\dagger \end{pmatrix} \\
&+ \begin{pmatrix} -\frac{\tilde{B}}{2}(i\Delta + \kappa/2)\bar{a}^* + i\tilde{A}\kappa\bar{a}^* & -\frac{\tilde{B}}{2}(i\Delta - \kappa/2)\bar{a} + i\tilde{A}\kappa\bar{a} \\ \frac{\tilde{B}}{2}(i\Delta + \kappa/2)\bar{a}^* - i\tilde{A}\kappa\bar{a}^* & \frac{\tilde{B}}{2}(i\Delta - \kappa/2)\bar{a} - i\tilde{A}\kappa\bar{a} \end{pmatrix} \begin{pmatrix} \hat{d} \\ \hat{d}^\dagger \end{pmatrix}.
\end{aligned} \tag{3.2}
$$

Using the cavity response function $\chi_c(\omega)$, Eq. (3.2) becomes

$$\begin{aligned}\begin{pmatrix}\hat{d}\\ \hat{d}^\dagger\end{pmatrix} = &-\sqrt{\kappa}\begin{pmatrix}\chi_c(\omega) & \\ & \chi_c^*(-\omega)\end{pmatrix}\begin{pmatrix}\hat{\xi}_{\text{in}}\\ \hat{\xi}_{\text{in}}^\dagger\end{pmatrix}\\ &+\begin{pmatrix}\chi_c(\omega)\left[-\frac{\tilde{B}}{2}(i\Delta+\kappa/2)\bar{a}+i\tilde{A}\kappa\bar{a}\right] & \chi_c(\omega)\left[-\frac{\tilde{B}}{2}(i\Delta+\kappa/2)\bar{a}+i\tilde{A}\kappa\bar{a}\right]\\ \chi_c^*(-\omega)\left[-\frac{\tilde{B}}{2}(-i\Delta+\kappa/2)\bar{a}^*-i\tilde{A}\kappa\bar{a}^*\right] & \chi_c^*(-\omega)\left[-\frac{\tilde{B}}{2}(-i\Delta+\kappa/2)\bar{a}^*-i\tilde{A}\kappa\bar{a}^*\right]\end{pmatrix}\begin{pmatrix}\hat{c}\\ \hat{c}^\dagger\end{pmatrix}\end{aligned} \tag{3.3}$$

and is inserted into

$$\begin{aligned}\begin{pmatrix}\chi_m^{-1}(\omega) & \\ & \chi_m^{*-1}(-\omega)\end{pmatrix}\begin{pmatrix}\hat{c}\\ \hat{c}^\dagger\end{pmatrix} = &-\sqrt{\gamma}\begin{pmatrix}\hat{\eta}\\ \hat{\eta}^\dagger\end{pmatrix}+\begin{pmatrix}-\frac{\tilde{B}}{2}\sqrt{\kappa}\bar{a}^* & \frac{\tilde{B}}{2}\sqrt{\kappa}\bar{a}\\ \frac{\tilde{B}}{2}\sqrt{\kappa}\bar{a}^* & -\frac{\tilde{B}}{2}\sqrt{\kappa}\bar{a}\end{pmatrix}\begin{pmatrix}\hat{\xi}_{\text{in}}\\ \hat{\xi}_{\text{in}}^\dagger\end{pmatrix}\\ &+\begin{pmatrix}-\frac{\tilde{B}}{2}(i\Delta+\kappa/2)\bar{a}^*+i\tilde{A}\kappa\bar{a}^* & -\frac{\tilde{B}}{2}(i\Delta-\kappa/2)\bar{a}+i\tilde{A}\kappa\bar{a}\\ \frac{\tilde{B}}{2}(i\Delta+\kappa/2)\bar{a}^*-i\tilde{A}\kappa\bar{a}^* & \frac{\tilde{B}}{2}(i\Delta-\kappa/2)\bar{a}-i\tilde{A}\kappa\bar{a}\end{pmatrix}\begin{pmatrix}\hat{d}\\ \hat{d}^\dagger\end{pmatrix},\end{aligned} \tag{3.4}$$

where $\chi_m(\omega) = [-i(\omega-\omega_m)+\gamma/2]^{-1}$ denotes the mechanical response function. This leads to

$$\begin{aligned}\begin{pmatrix}\chi_m^{-1}(\omega) & \\ & \chi_m^{*-1}(-\omega)\end{pmatrix}\begin{pmatrix}\hat{c}\\ \hat{c}^\dagger\end{pmatrix} = &-\sqrt{\gamma}\begin{pmatrix}\hat{\eta}\\ \hat{\eta}^\dagger\end{pmatrix}-\sqrt{\kappa}\begin{pmatrix}\bar{a}^*\alpha(\omega) & -\bar{a}\alpha^*(-\omega)\\ -\bar{a}^*\alpha(\omega) & \bar{a}\alpha^*(-\omega)\end{pmatrix}\begin{pmatrix}\hat{\xi}_{\text{in}}\\ \hat{\xi}_{\text{in}}^\dagger\end{pmatrix}\\ &+\begin{pmatrix}-i\Sigma(\omega) & -i\Sigma(\omega)\\ i\Sigma(\omega) & i\Sigma(\omega)\end{pmatrix}\begin{pmatrix}\hat{c}\\ \hat{c}^\dagger\end{pmatrix},\end{aligned} \tag{3.5}$$

where we defined the auxiliary function $\alpha(\omega)$ and the optomechanical self-energy $\Sigma(\omega)$ as

$$\begin{aligned}\Sigma(\omega) &= \Sigma_{\tilde{A}}(\omega)+\Sigma_{\tilde{B}}(\omega)+\Sigma_{\tilde{A}\tilde{B}}(\omega)\\ \alpha(\omega) &= \alpha_{\tilde{A}}(\omega)+\alpha_{\tilde{B}}(\omega),\end{aligned} \tag{3.6}$$

with

$$\begin{aligned}\Sigma_{\tilde{A}}(\omega) &= -i(\tilde{A}\kappa|\bar{a}|)^2\left[\chi_c(\omega)-\chi_c^*(-\omega)\right]\\ \Sigma_{\tilde{B}}(\omega) &= i\left(\frac{\tilde{B}}{2}\right)^2|\bar{a}|^2\left[\chi_c(\omega)\left(i\Delta+\frac{\kappa}{2}\right)^2-\chi_c^*(-\omega)\left(i\Delta-\frac{\kappa}{2}\right)^2\right]\\ \Sigma_{\tilde{A}\tilde{B}}(\omega) &= \tilde{B}\tilde{A}\kappa\,|\bar{a}|^2\left[\chi_c(\omega)\left(i\Delta+\frac{\kappa}{2}\right)-\chi_c^*(-\omega)\left(i\Delta-\frac{\kappa}{2}\right)\right]\end{aligned} \tag{3.7}$$

and

$$\begin{aligned}\alpha_{\tilde{A}}(\omega) &= i\chi_c(\omega)\tilde{A}\kappa\\ \alpha_{\tilde{B}}(\omega) &= \frac{\tilde{B}}{2}-\frac{\tilde{B}}{2}\chi_c(\omega)\left(i\Delta+\frac{\kappa}{2}\right).\end{aligned} \tag{3.8}$$

In the purely dispersive case ($\tilde{B}=0$) the above definition of the optomechanical self-energy $\Sigma(\omega)$ reproduces the notation used in [8]. Defining $\Sigma_{\tilde{B}}(\omega)$ and $\Sigma_{\tilde{A}\tilde{B}}(\omega)$ in a similar fashion, we can deduce the optical damping $\gamma_{\text{opt}} = -2\text{Im}[\Sigma(\omega_m)]$ and frequency shift $\delta\omega_m = \text{Re}[\Sigma(\omega_m)]$. Note that this means that $\Sigma_{\tilde{B}}(\omega)$ differs from the definition in [16] by a factor of $-2i\omega_m\chi_m^*(-\omega)$. Furthermore, each term of the optomechanical self-energy fulfils $\Sigma_{\tilde{X}}^*(\omega) = \Sigma_{\tilde{X}}(-\omega)$. This allows to use this property for $\Sigma(\omega)$ in Section 3.2 without specifying in the first place, weather purely dispersive, purely dissipative or mixed coupling is treated.

Finally, note that the definition of $\alpha(\omega)$ is connected to the weak-coupling force spectrum, i.e. $\kappa|\bar{a}|^2|\alpha(\omega)|^2 = S_{FF}(\omega)x_0^2$. This relation is valid independent of the type of the applied coupling.

The solution for the mechanical mode $\hat{c}$ is achieved from

$$\begin{pmatrix} \chi_m^{-1}(\omega) + i\Sigma(\omega) & i\Sigma(\omega) \\ -i\Sigma(\omega) & \chi_m^{*-1}(-\omega) - i\Sigma(\omega) \end{pmatrix} \begin{pmatrix} \hat{c} \\ \hat{c}^\dagger \end{pmatrix} = -\sqrt{\gamma} \begin{pmatrix} \hat{\eta} \\ \hat{\eta}^\dagger \end{pmatrix} - \sqrt{\kappa} \begin{pmatrix} \bar{a}^*\alpha(\omega) & -\bar{a}\alpha^*(-\omega) \\ -\bar{a}^*\alpha(\omega) & \bar{a}\alpha^*(-\omega) \end{pmatrix} \begin{pmatrix} \hat{\xi}_{\text{in}} \\ \hat{\xi}_{\text{in}}^\dagger \end{pmatrix} \tag{3.9}$$

by calculating the inverse of the matrix on the left. Denoting the determinant of this matrix as $\mathscr{N}(\omega) = \chi_m^{-1}(\omega)\chi_m^{*-1}(-\omega) + 2\omega_m\Sigma(\omega)$, the result is given by

$$\begin{aligned} \begin{pmatrix} \hat{c} \\ \hat{c}^\dagger \end{pmatrix} = &- \frac{\sqrt{\gamma}}{\mathscr{N}(\omega)} \begin{pmatrix} \chi_m^{*-1}(-\omega) - i\Sigma(\omega) & -i\Sigma(\omega) \\ i\Sigma(\omega) & \chi_m^{-1}(\omega) + i\Sigma(\omega) \end{pmatrix} \begin{pmatrix} \hat{\eta} \\ \hat{\eta}^\dagger \end{pmatrix} \\ &- \frac{\sqrt{\kappa}}{\mathscr{N}(\omega)} \begin{pmatrix} \chi_m^{*-1}(-\omega)\bar{a}^*\alpha(\omega) & -\chi_m^{*-1}(-\omega)\bar{a}\alpha^*(-\omega) \\ -\chi_m^{-1}(\omega)\bar{a}^*\alpha(\omega) & \chi_m^{-1}(\omega)\bar{a}\alpha^*(-\omega) \end{pmatrix} \begin{pmatrix} \hat{\xi}_{\text{in}} \\ \hat{\xi}_{\text{in}}^\dagger \end{pmatrix}. \end{aligned} \tag{3.10}$$

The solution for the optical mode is obtained by substituting Eq. (3.10) into Eq. (3.3),

$$\begin{aligned} \begin{pmatrix} \hat{d} \\ \hat{d}^\dagger \end{pmatrix} = &-\sqrt{\kappa} \begin{pmatrix} \chi_c(\omega) & \\ & \chi_c^*(-\omega) \end{pmatrix} \begin{pmatrix} \hat{\xi}_{\text{in}} \\ \hat{\xi}_{\text{in}}^\dagger \end{pmatrix} \\ &+ \frac{\sqrt{\gamma}}{\mathscr{N}(\omega)} \begin{pmatrix} \bar{a}\left[\frac{\tilde{B}}{2} - \alpha(\omega)\right]\chi_m^{*-1}(-\omega) & \bar{a}\left[\frac{\tilde{B}}{2} - \alpha(\omega)\right]\chi_m^{-1}(\omega) \\ \bar{a}^*\left[\frac{\tilde{B}}{2} - \alpha^*(-\omega)\right]\chi_m^{*-1}(-\omega) & \bar{a}^*\left[\frac{\tilde{B}}{2} - \alpha^*(-\omega)\right]\chi_m^{-1}(\omega) \end{pmatrix} \begin{pmatrix} \hat{\eta} \\ \hat{\eta}^\dagger \end{pmatrix} \\ &- \frac{\sqrt{\kappa}}{\mathscr{N}(\omega)} \begin{pmatrix} 2i\omega_m|\bar{a}|^2\left[\frac{\tilde{B}}{2} - \alpha(\omega)\right]\alpha(\omega) & -2i\omega_m\bar{a}^2\left[\frac{\tilde{B}}{2} - \alpha(\omega)\right]\alpha^*(-\omega) \\ 2i\omega_m\bar{a}^{*2}\left[\frac{\tilde{B}}{2} - \alpha^*(-\omega)\right]\alpha(\omega) & -2i\omega_m|\bar{a}|^2\left[\frac{\tilde{B}}{2} - \alpha^*(-\omega)\right]\alpha^*(-\omega) \end{pmatrix} \begin{pmatrix} \hat{\xi}_{\text{in}} \\ \hat{\xi}_{\text{in}}^\dagger \end{pmatrix}. \end{aligned} \tag{3.11}$$

Remarkably, the exact solutions of the linearized equations of motion, Eqs. (3.10) and (3.11), have the same structure for both types of coupling. Apart from an additional contribution proportional to $\tilde{B}$ in Eq. (3.11), differences are hidden in the functions $\Sigma(\omega)$ and $\alpha(\omega)$. The additional dependence of $\Sigma_{\tilde{B}}(\omega)$, $\Sigma_{\tilde{A}\tilde{B}}(\omega)$ and $\alpha_{\tilde{B}}(\omega)$ on the detuning Δ arises since, for dissipative coupling, the equations of motion (1.9) and (1.10) contain a term proportional to the drive strength Ω. The constant term in $\alpha_{\tilde{B}}(\omega)$ is due to the direct interaction between the optical bath and the mechanical mode.

Finally, the fluctuations of the optical output are obtained by using $\hat{a}_{\text{out}} = (\bar{a}_{\text{out}} + \hat{\xi}_{\text{out}})e^{-i\omega_d t}$ and linearizing the input-output relation (1.4),

$$\hat{\xi}_{\text{in}} - \hat{\xi}_{\text{out}} = -\sqrt{\kappa}\hat{d} - \sqrt{\kappa}\bar{a}\frac{\tilde{B}}{2}\frac{\hat{x}}{x_0}. \tag{3.12}$$

Then, with Eqs. (3.10) and (3.11), we find

$$\begin{pmatrix}\hat{\xi}_{\text{out}}\\ \hat{\xi}^\dagger_{\text{out}}\end{pmatrix} = \begin{pmatrix}1-\kappa\chi_c(\omega) & \\ & 1-\kappa\chi_c^*(-\omega)\end{pmatrix}\begin{pmatrix}\hat{\xi}_{\text{in}}\\ \hat{\xi}^\dagger_{\text{in}}\end{pmatrix} - \frac{\sqrt{\gamma}\sqrt{\kappa}\bar{a}}{\mathscr{N}(\omega)}\begin{pmatrix}\chi_m^{-1*}(-\omega)\alpha(\omega) & \chi_m^{-1}(\omega)\alpha(\omega)\\ \chi_m^{-1*}(-\omega)\alpha^*(-\omega) & \chi_m^{-1}(\omega)\alpha^*(-\omega)\end{pmatrix}\begin{pmatrix}\hat{\eta}\\ \hat{\eta}^\dagger\end{pmatrix}$$
$$+\frac{2i\kappa\omega_m}{\mathscr{N}(\omega)}\begin{pmatrix}|\bar{a}|^2\alpha(\omega)^2 & -\bar{a}^2\alpha(\omega)\alpha^*(-\omega)\\ -(\bar{a}^*)^2\alpha(\omega)\alpha^*(-\omega) & |\bar{a}|^2\alpha^*(-\omega)^2\end{pmatrix}\begin{pmatrix}\hat{\xi}_{\text{in}}\\ \hat{\xi}^\dagger_{\text{in}}\end{pmatrix}. \tag{3.13}$$

Note that in obtaining this result, we made use of $\mathscr{N}(\omega) = \mathscr{N}^*(-\omega)$ which is a consequence of the same property of the optomechanical self-energy $\Sigma(\omega)$.

In the following sections and chapters we will use Eqs. (3.10), (3.11), and (3.13) e.g. to calculate different spectra. However, in the case of purely dispersive coupling it is well-known that unstable parameter regions exist where the linearization is not justified and thus the solutions of the linearized equations are not appropriate to describe the system. In the case of dissipative coupling, we know from the weak-coupling description (cf. Chapter 2) that two unstable regions exist due to the criterion $\gamma_{\text{tot}} < 0$. To assure our strong-coupling results we determine the stability of the linearized equations of motion.

In the time-domain, the system is described by four linear differential equations, i.e. the linearized equations of motion (1.15) and (1.16), and their hermitian conjugates. Written in a concise way, this system of differential equations is given by

$$\frac{d}{dt}\begin{pmatrix}\hat{d}\\ \hat{d}^\dagger\\ \hat{c}\\ \hat{c}^\dagger\end{pmatrix} = \boldsymbol{M}\begin{pmatrix}\hat{d}\\ \hat{d}^\dagger\\ \hat{c}\\ \hat{c}^\dagger\end{pmatrix} + \boldsymbol{F}\begin{pmatrix}\hat{\xi}_{\text{in}}\\ \hat{\xi}^\dagger_{\text{in}}\\ \hat{\eta}\\ \hat{\eta}^\dagger\end{pmatrix}, \tag{3.14}$$

where the matrices $\boldsymbol{M}$ and $\boldsymbol{F}$ are defined as

$$\boldsymbol{M} = \begin{pmatrix} i\Delta-\frac{\kappa}{2} & 0 & i\tilde{A}\kappa\bar{a}-\frac{\tilde{B}}{2}\left(i\Delta+\frac{\kappa}{2}\right)\bar{a} & i\tilde{A}\kappa\bar{a}-\frac{\tilde{B}}{2}\left(i\Delta+\frac{\kappa}{2}\right)\bar{a}\\ 0 & -i\Delta-\frac{\kappa}{2} & -i\tilde{A}\kappa\bar{a}^*+\frac{\tilde{B}}{2}\left(i\Delta-\frac{\kappa}{2}\right)\bar{a}^* & -i\tilde{A}\kappa\bar{a}^*+\frac{\tilde{B}}{2}\left(i\Delta-\frac{\kappa}{2}\right)\bar{a}^*\\ i\tilde{A}\kappa\bar{a}^*-\frac{\tilde{B}}{2}\left(i\Delta+\frac{\kappa}{2}\right)\bar{a}^* & i\tilde{A}\kappa\bar{a}-\frac{\tilde{B}}{2}\left(i\Delta-\frac{\kappa}{2}\right)\bar{a} & -i\omega_m-\frac{\gamma}{2} & 0\\ -i\tilde{A}\kappa\bar{a}^*+\frac{\tilde{B}}{2}\left(i\Delta+\frac{\kappa}{2}\right)\bar{a}^* & -i\tilde{A}\kappa\bar{a}+\frac{\tilde{B}}{2}\left(i\Delta-\frac{\kappa}{2}\right)\bar{a} & 0 & i\omega_m-\frac{\gamma}{2}\end{pmatrix} \tag{3.15}$$

and

$$\boldsymbol{F} = -\begin{pmatrix}\sqrt{\kappa} & 0 & 0 & 0\\ 0 & \sqrt{\kappa} & 0 & 0\\ \frac{\tilde{B}}{2}\sqrt{\kappa}\bar{a}^* & -\frac{\tilde{B}}{2}\sqrt{\kappa}\bar{a} & \sqrt{\gamma} & 0\\ -\frac{\tilde{B}}{2}\sqrt{\kappa}\bar{a}^* & \frac{\tilde{B}}{2}\sqrt{\kappa}\bar{a} & 0 & \sqrt{\gamma}\end{pmatrix}. \tag{3.16}$$

The solution of Eq. (3.14) is stable, if the real part of all eigenvalues of $\boldsymbol{M}$ is negative. Using the Routh-Hurwitz criterion, conditions for the parameters appearing in $\boldsymbol{M}$ can be derived. However, for our purpose it is sufficient to numerically calculate the eigenvalues for the set of parameters used throughout this work. Results of this calculations can be seen in Figs. 3.1 (a) and 3.4. In summary, for dissipative coupling, we find two regions of instability in good agreement with the condition $\gamma_{\text{tot}} < 0$. Furthermore, very strong coupling leads to a third unstable region that is not predicted by the weak-coupling approach, i.e. it corresponds to a parameter set where $\gamma_{\mathrm{tot}} > 0$. This, however, is not unique to dissipative coupling. Very strong dispersive coupling leads an additional unstable region as well.

3.2. Mechanical spectrum

Using the exact solution of the mechanical mode, Eq. (3.10), we calculate the mechanical spectrum $S_{cc}(\omega) = \int_{-\infty}^{+\infty} \frac{d\omega'}{2\pi} \langle \hat{c}^\dagger(\omega)\hat{c}(\omega')\rangle$ with the help of the known expectation values of the input modes $\hat{\xi}_{\mathrm{in}}$ and $\hat{\eta}$,

$$\begin{aligned} \langle \hat{\xi}_{\mathrm{in}}(\omega)\hat{\xi}^\dagger_{\mathrm{in}}(\omega')\rangle &= 2\pi\delta(\omega+\omega') \\ \langle \hat{\eta}^\dagger(\omega)\hat{\eta}(\omega')\rangle &= 2\pi n_{\mathrm{th}}\delta(\omega+\omega') \\ \langle \hat{\eta}(\omega)\hat{\eta}^\dagger(\omega')\rangle &= 2\pi\left(n_{\mathrm{th}}+1\right)\delta(\omega+\omega'). \end{aligned} \tag{3.17}$$

The expectation values of all other combinations of two input modes are zero. Then,

$$\begin{aligned} S_{cc}(\omega) = \int\limits_{-\infty}^{+\infty} \frac{d\omega'}{2\pi} \Bigg\{ &\frac{\gamma}{\mathcal{N}(\omega)\mathcal{N}(\omega')}\Sigma(\omega)\Sigma(\omega')\langle\hat{\eta}(\omega)\hat{\eta}^\dagger(\omega')\rangle \\ &+ \frac{\gamma}{\mathcal{N}(\omega)\mathcal{N}(\omega')}\left[\chi_m^{-1}(\omega)+i\Sigma(\omega)\right]\left[\chi_m^{*-1}(\omega')-i\Sigma(\omega')\right]\langle\hat{\eta}^\dagger(\omega)\hat{\eta}(\omega')\rangle \\ &\frac{\kappa}{\mathcal{N}(\omega)\mathcal{N}(\omega')}|\bar{a}|^2\chi_m^{-1}(\omega)\alpha(\omega)\chi_m^{*-1}(\omega')\alpha^*(-\omega')\langle\hat{\xi}_{\mathrm{in}}(\omega)\hat{\xi}^\dagger_{\mathrm{in}}(\omega')\rangle \Bigg\}, \end{aligned} \tag{3.18}$$

and taking advantage of $\Sigma(-\omega) = \Sigma(\omega)^*$, this simplifies to

$$S_{cc}(\omega) = \frac{\gamma\sigma_{\mathrm{th}}(\omega) + \kappa\sigma_{\mathrm{opt}}(\omega)}{|\mathcal{N}(\omega)|^2}, \tag{3.19}$$

where $\sigma_{\mathrm{th}}(\omega) = |\Sigma(\omega)|^2\,(n_{\mathrm{th}}+1) + \left|\chi_m^{-1}(\omega)+i\Sigma(\omega)\right|^2 n_{\mathrm{th}}$ and $\sigma_{\mathrm{opt}}(\omega) = \left|\chi_m^{-1}(\omega)\right|^2|\bar{a}|^2|\alpha(\omega)|^2$. This result is valid for purely dispersive, purely dissipative and both types of coupling but has the same form as found in the case of dispersive coupling only [8]. For $\tilde{B} = 0$ the result coincides with [8]; setting $\tilde{A} = 0$ the result coincides with [16].

Figure 3.1 (a) shows the mechanical spectrum $S_{cc}(\omega)$ for strong dissipative coupling. Dark areas indicate regions where the solutions of the linearized equations of motion are unstable. This was numerically tested for the parameters used in Fig. 3.1 and coincides with the regions where the total damping rate γ_{tot} from the weak-coupling approach is negative. Whereas dispersive coupling leads to one unstable region for blue detuning, dissipative coupling can lead to a second unstable region for red detuning in addition to an unstable region for blue detuning. A third unstable region exists for even stronger drive or large red detuning. This is not predicted by the behaviour of the optical damping rate, i.e. it appears although $\gamma_{\mathrm{tot}} > 0$.

Focusing on the stable regions, we find two prominent features. First, at $\Delta = \Delta_{\mathrm{opt}} = \omega_m/2$ a strong decrease of the phonon number $\langle\hat{n}\rangle = \int d\omega S_{cc}(\omega)/2\pi$ can be observed.

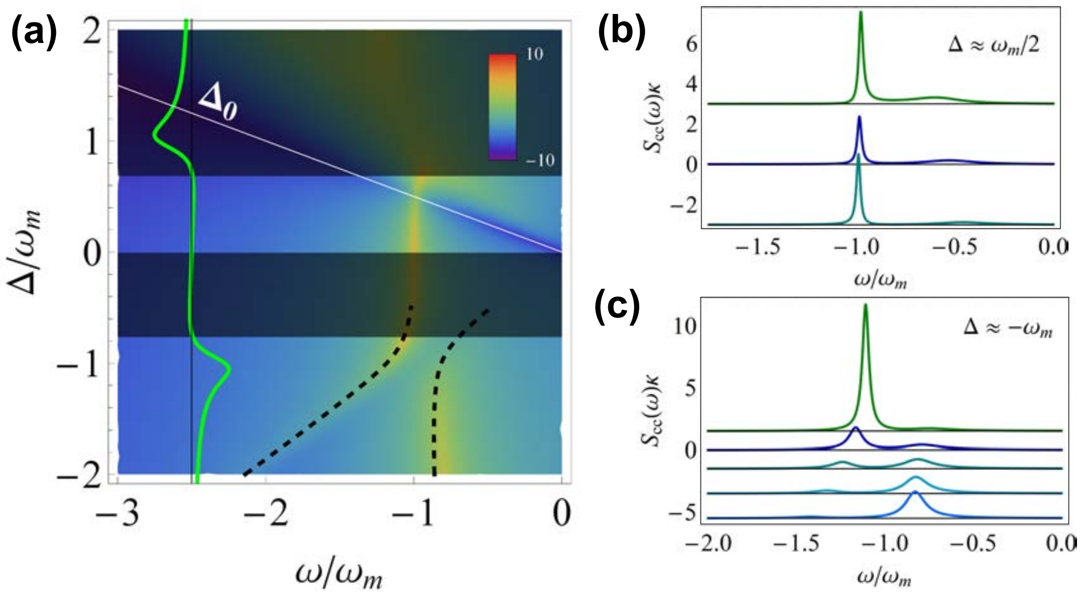

Figure 3.1.: (a) Logarithm of the mechanical spectrum $S_{cc}(\omega)\kappa$ as a function of detuning Δ. Parameters are $\omega_m/\kappa = 3$, $\omega_m/\gamma = 10^5$, $n_{\mathrm{th}} = 100$, $\tilde{A} = 0$, and $\tilde{B}\bar{a} = 0.4$. The dark regions indicate regions of instability obtained from a numerical calculation. The green curve gives half of the total damping rate, $\gamma_{\mathrm{tot}}/2$, obtained from the quantum noise approach with the origin shifted to $(-2.5, 0)$. The dashed lines show the real parts of the eigenvalues of the Hamiltonian (3.20). (b) $S_{cc}(\omega)\kappa$ for detunings $\Delta/\omega_m = 0.55, 0.5, 0.45$ (from top to bottom). (c) $S_{cc}(\omega)\kappa$ for detunings $\Delta/\omega_m = -0.9, -1, -1.1, -1.2, -1.3$ (from top to bottom).

As mentioned in Chapter 2, this detuning is associated with cooling [16] and a special case of the strong modifications of the mechanical spectrum at $\Delta_0(\omega)$. If $\Delta = \Delta_0(\omega)$, the force spectrum $S_{FF}(\omega)$ vanishes, which means that at this frequency ω only the first term of Eq. (3.19), $\sigma_{\mathrm{th}}(\omega)$, contributes to $S_{cc}(\omega)$. Furthermore, Fig. 3.1 (b) shows that, apart from the main peak close to the mechanical resonance $\omega = -\omega_m$, there is a broad contribution at a second frequency arising from $\sigma_{\mathrm{opt}}(\omega)/|\mathcal{N}(\omega)|^2$. It is given as a trade-off between the maximum of the Fano line shape of the force spectrum $S_{FF}(\omega)$ at $\omega = \frac{-4\Delta^2+\kappa^2}{4\Delta}$ and the peak of $|\mathcal{N}(\omega)|^{-2}$ at $\omega = -\omega_m$. It is this contribution, away from the mechanical resonance frequency, that finally limits the cooling due to its increasing relevance with increasing coupling strength.

The second feature is found at $\Delta = -\omega_m$. Similar to the case of dispersive coupling, we find normal-mode splitting even though slight quantitative differences appear. In the following we use a simplified Hamiltonian to find an approximation that describes the splitting. Recall that dissipative coupling leads to two terms in the equations of motion (1.9) and (1.10). We neglect the term proportional to the damping rate, i.e. the direct influence of the optical bath on the mechanical oscillator, and only take the effect proportional to the drive Ω into account. Furthermore, we use the rotating wave approximation and neglect the fast rotating terms $\hat{d}^\dagger \hat{c}^\dagger$ and $\hat{d}\hat{c}$. Then, in the rotating frame, the simplified, non-hermitian Hamiltonian is given by

$$\hat{H} = -\left(\Delta + i\frac{\kappa}{2}\right)\hat{d}^\dagger \hat{d} + \left(\omega_m - i\frac{\gamma}{2}\right)\hat{c}^\dagger \hat{c} + \left[\left(\frac{\tilde{B}\Omega}{2} - \tilde{A}\bar{a}\kappa\right)\hat{c}\hat{d}^\dagger + \text{H.c.}\right]. \tag{3.20}$$

Note that using this approximation, the difference between purely dispersive and purely dissipative coupling only depends on whether the drive strength Ω or the intra-cavity amplitude $\bar{a}$ is fixed. Fixing Ω for purely dissipative and $\bar{a}$ for purely dispersive coupling leads to similar results. Instead fixing one parameter for both types of coupling, as done here with a variable drive strength Ω and a fixed $\bar{a}$, leads to modifications of the splitting due to an additional dependence on the detuning Δ. Since it is not possible to fix both Ω and $\bar{a}$ at the same time, mixed coupling will always lead to Δ-dependent modifications arising from either the dissipative or the dispersive term.

In the general case of dispersive and dissipative coupling, the eigenvalues of the simplified Hamiltonian (3.20) can be calculated as

$$\begin{aligned} E_\pm = & -i\frac{\gamma+\kappa}{4} + \frac{\omega_m - \Delta}{2} \\ & \pm \sqrt{-\left[\gamma - \kappa + 2i\left(\Delta + \omega_m\right)\right]^2 + |\bar{a}|^2\left[16(\tilde{A}^2\kappa^2 - \tilde{A}\tilde{B}\Delta\kappa) + \tilde{B}^2\left(4\Delta^2 + \kappa^2\right)\right]}. \end{aligned} \tag{3.21}$$

The energies corresponding to the two modes are the real parts of these eigenvalues $E_\pm$, whereas the imaginary parts contain information about the associated linewidths. We show the real parts of the eigenvalues (calculated for $\tilde{A} = 0$) in Fig. 3.1 (a) and, despite the simplifications, the energies fit the peak position of the spectrum very well. Differences to purely dispersive coupling arise since the dispersive coupling matrix element is constant for fixed values of the cavity amplitude $\bar{a}$. In contrast, the dissipative coupling matrix element depends on the drive strength Ω, which is a function of detuning Δ if $\bar{a}$ is fixed. This affects the curvature of the modes and leads to Δ-dependent width of the splitting. Moreover, the eigenvalues of the simplified Hamiltonian indicate that, in the case of purely dissipative coupling, the splitting is no longer minimal at $\Delta = -\omega_m$. Neglecting the damping terms in the Hamiltonian (3.20), the minimal splitting occurs at $\Delta = -\omega_m/(1 + \tilde{B}^2|\bar{a}|^2)$. Figure 3.1 (c) shows in detail how the single peak at the mechanical frequency is split due to the optomechanical coupling.

We further investigate the eigenvalues $E_\pm$ from Eq. (3.21) to clarify at which coupling strength normal-mode splitting appears in the mechanical spectrum $S_{cc}(\omega)$. Figure 3.2 (a) shows that $\text{Re}[E_\pm]$ coincide well with the peak positions of the mechanical spectrum as a function of coupling strength $\tilde{B}\bar{a}$. If $\Delta = -\omega_m$, small coupling corresponds to degenerate energies, i.e. $\text{Re}[E_+] = \text{Re}[E_-]$. In this case, the argument of the square root in Eq. (3.21) is real and negative. Thus, for small coupling, the root contributes

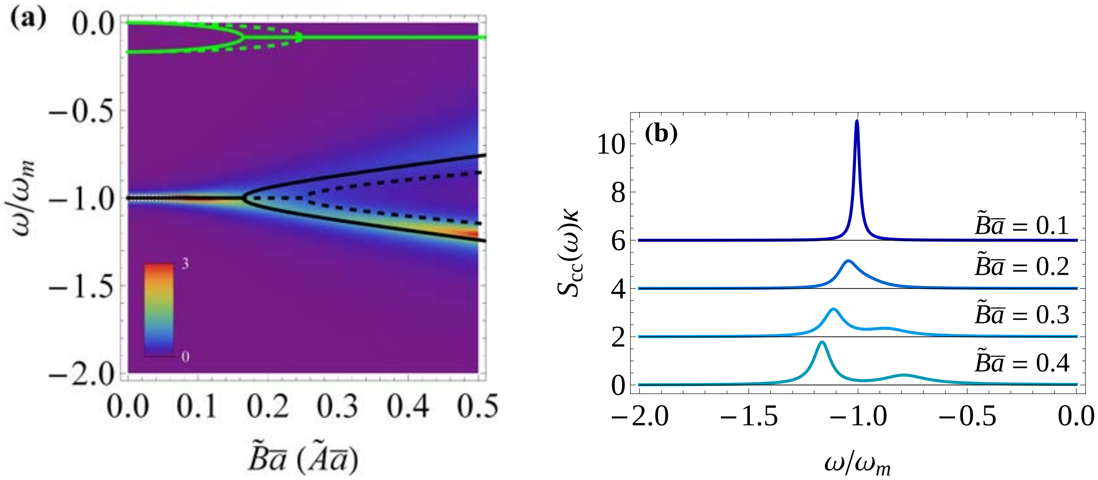

Figure 3.2.: (a) Real part (black curves) and imaginary part (green curves) of the eigenvalues $E_\pm$ calculated from the Hamiltonian (3.20) as a function of coupling strength. Solid (dashed) lines indicate purely dissipative (dispersive) coupling. The plot is underlaid with the mechanical spectrum $S_{cc}(\omega)\kappa$ as a function of coupling strength $\tilde{B}\bar{a}$ for $\Delta = -\omega_m$ and $\tilde{A} = 0$. Other parameters are $\omega_m/\kappa = 3$, $\omega_m/\gamma = 10^5$, and $n_{\text{th}} = 100$. (b) Mechanical spectrum $S_{cc}(\omega)$ at $\Delta = -\omega_m$ for different coupling strengths $\tilde{B}\bar{a}$ between 0.1 and 0.4 in absence of dispersive coupling ($\tilde{A} = 0$).

only to the imaginary part of the eigenvalues and affects the linewidths given by κ and γ respectively. With increasing coupling strength the linewidths approach their mean value $(\kappa+\gamma)/2$, which is reached where the root becomes zero. Then the modes $\text{Re}[E_\pm]$ start to split whereas the linewidths remain unchanged. In case of purely dissipative coupling at $\Delta = -\omega_m$, the critical coupling strength where mode-splitting starts is given by $\tilde{B}|\bar{a}| = (\kappa-\gamma)/\sqrt{4\omega_m^2+\kappa^2}$.

Furthermore, Fig. 3.2 (a) shows the approximated normal-mode splitting for purely dispersive and purely dissipative coupling. For the set of parameters used, normal-mode splitting due to dispersive coupling starts at a larger coupling strength than the splitting obtained for purely dissipative coupling. Note, however, that this depends on the sideband parameter ω_m/κ, since the critical dispersive coupling strength at $\Delta = -\omega_m$ is given by $\tilde{A}|\bar{a}| = (\kappa-\gamma)/(4\kappa)$. Thus, for $\omega_m^2/\kappa^2 < 15/4$, dispersive coupling would lead to normal-mode splitting at a smaller coupling strength than dissipative coupling.

Finally note that if $\Delta \neq -\omega_m$, the root in Eq. (3.21) is complex valued and the modes start with a finite energy separation from the uncoupled case.

3.3. Optical spectra

The optical spectra, especially the optical output spectrum, are experimentally easier accessible than the mechanical spectrum. Purely dispersive coupling allows interaction between the mechanical element and the optical output only via the cavity, such that $S_{dd}^{\rm out}(\omega) = \kappa S_{dd}(\omega)$. Note that this is no longer the case for dissipative coupling since there is direct influence of the mechanical oscillator on the output which is not mediated by the cavity. Thus, we use the full solutions (3.11) and (3.13) to calculate both the cavity and the optical output spectrum. Then, applying Eq. (3.17), we find

$$S_{dd}(\omega) = \frac{|\bar{a}|^2|\alpha(-\omega) - \tilde{B}/2)|^2}{|\mathcal{N}(\omega)|^2}\left[4\kappa|\bar{a}|^2\omega_m^2|\alpha(\omega)|^2 + \gamma|\chi_m^{-1}(-\omega)|^2(n_{\rm th}+1) + \gamma|\chi_m^{-1}(\omega)|^2 n_{\rm th}\right] \tag{3.22}$$

and

$$S_{dd}^{\rm out}(\omega) = \kappa\frac{|\alpha(-\omega)|^2}{|\alpha(-\omega) - \tilde{B}/2|^2}S_{dd}(\omega). \tag{3.23}$$

Apart from the factor κ, these two spectra differ by the subtraction of the constant term from $\alpha(-\omega)$. Recalling the definition of $\alpha(\omega)$, Eq. (3.8), this means that dissipative coupling contributes to the cavity spectrum $S_{dd}(\omega)$ only at frequencies filtered by the cavity response $|\chi_c(-\omega)|^2$. This leads to the enhancement of the lower sideband for $\Delta < 0$ and of the upper sideband if $\Delta > 0$, similar to the case of dispersive coupling. In addition, due to the direct influence of the mechanical oscillator on the optical output, dissipative coupling leads to a contribution to the output spectrum $S_{dd}^{\rm out}(\omega)$ that is not filtered by the cavity response. This is hidden in the definition of $\alpha(-\omega)$ in Eq. (3.8). Figure 3.3 illustrates the differences of the cavity spectrum (in units of κ) $S_{dd}(\omega)\kappa$ and the optical output spectrum $S_{dd}^{\rm out}(\omega)$ in the case of dissipative coupling, whereas for purely dispersive coupling $S_{dd}(\omega)\kappa$ and $S_{dd}^{\rm out}(\omega)$ are the same.

The optical output spectrum is connected to the displacement spectrum $S_{xx}(\omega)$ via $S_{dd}^{\rm out}(\omega) = S_{FF}(-\omega)S_{xx}(\omega)$ [16]. Thus, it is possible to observe the features of the mechanical spectrum $S_{cc}(\omega)$ in the optical output spectrum. As shown in Fig. 3.4 (b) we recover normal-mode splitting at $\Delta = -\omega_m$ and find modifications of the optical output spectrum $S_{dd}^{\rm out}(\omega)$ for $\Delta = \Delta_0(\pm\omega)$. First, we can see the influence of Δ_0 on the mechanical spectrum $S_{cc}(\omega)$ at $\Delta = \Delta_0(+\omega)$. Moreover, there is also the direct influence through the weak-coupling force spectrum $S_{FF}(-\omega)$, i.e. the optical output spectrum becomes exactly zero if $\Delta = \Delta_0(-\omega)$. Figure 3.4 (a) shows $S_{dd}^{\rm out}(\omega)$ in the case of purely dispersive coupling for comparison. Normal-mode splitting can be observed as well, but for purely dispersive coupling the detuning Δ_0 has no special role. Note also the different instability regions of the optical output spectrum, depending on the type of coupling.

For mixed coupling (i.e. $\tilde{A} \neq 0$ and $\tilde{B} \neq 0$) the new features of dissipative coupling are modified but do not disappear. In particular, there is a detuning $\Delta_0(\omega)$ such that $S_{FF}(\omega) = 0$, cf. Eq. (2.4). However, its offset $\kappa\tilde{A}/\tilde{B}$ depends on the ratio of the couplings and leads to a shift of Δ_0 compared to the purely dissipative case. Furthermore, mixed coupling modifies the regions where $\gamma_{\rm tot} < 0$ in the weak-coupling approach and the corresponding changes of the unstable regions are captured by the numerical calculation.

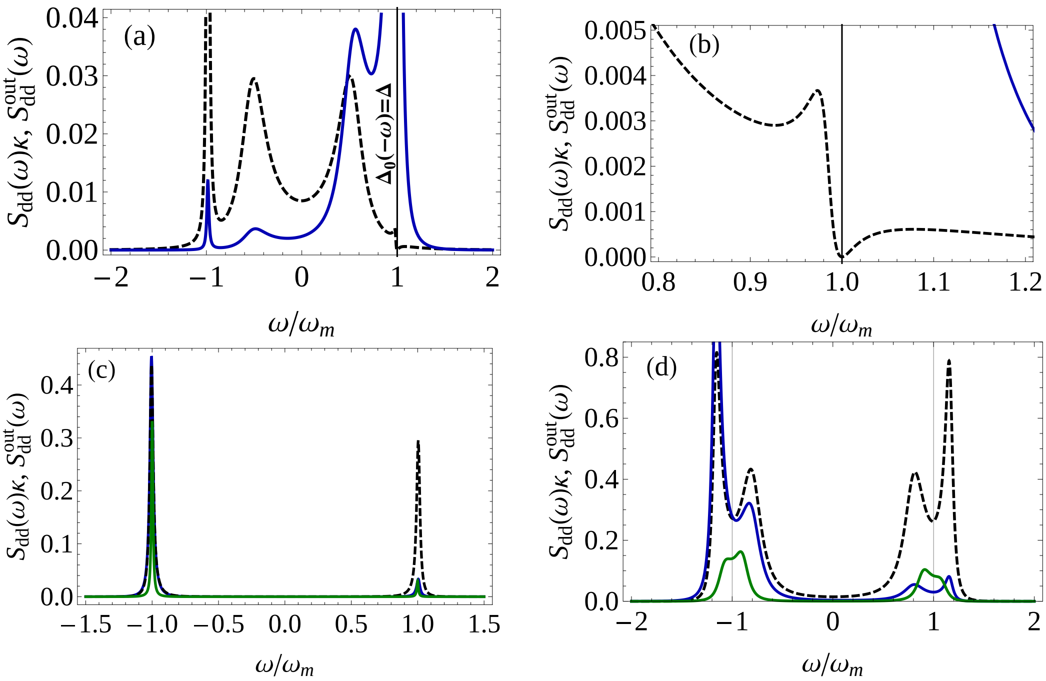

Figure 3.3.: (a) shows the cavity spectrum $S_{dd}(\omega)\kappa$ (blue solid line) and the optical output spectrum $S_{dd}^{\text{out}}(\omega)$ for purely dissipative coupling $\tilde{B}\bar{a} = 0.4$, $\tilde{A} = 0$ at detuning $\Delta = \omega_m/2$. (b) shows the section of (a) close to $\omega = \omega_m$, where the optical output spectrum becomes exactly zero. (c) and (d) show the cavity spectrum $S_{dd}(\omega)\kappa$ (blue solid line) and the optical output spectrum $S_{dd}^{\text{out}}(\omega)$ for purely dissipative coupling, and the cavity spectrum $S_{dd}(\omega)\kappa$ for purely dispersive coupling (green solid line) at detuning $\Delta = -\omega_m$. The coupling strength is either 0.1 (c) or 0.4 (d). All other parameter of this figure are the same as in Fig. 3.1.

3.4. Cooling in the strong-coupling limit

As mentioned in Section 3.2, the mean phonon number $\langle \hat{n} \rangle = \langle \hat{c}^\dagger \hat{c} \rangle$ can be obtained from the mechanical spectrum $S_{cc}(\omega)$ by integration. In contrast to the weak-coupling result, the mechanical spectrum calculated from the exact solutions to the linearized equations of motion indicates that cooling at $\Delta = \Delta_{\text{opt}}$ is limited [16]. This was already mentioned in Section 3.2 where we discussed the contribution to $S_{cc}(\omega)$ away from $\omega = -\omega_m$ shown in Fig. 3.1 (b). It is a consequence of the Fano line shape in the force spectrum $S_{FF}(\omega)$ which leads to complete destructive noise-interference only exactly at the mechanical frequency ω_m.

To obtain an analytical expression for the final phonon number $\langle \hat{n} \rangle$, we make use of

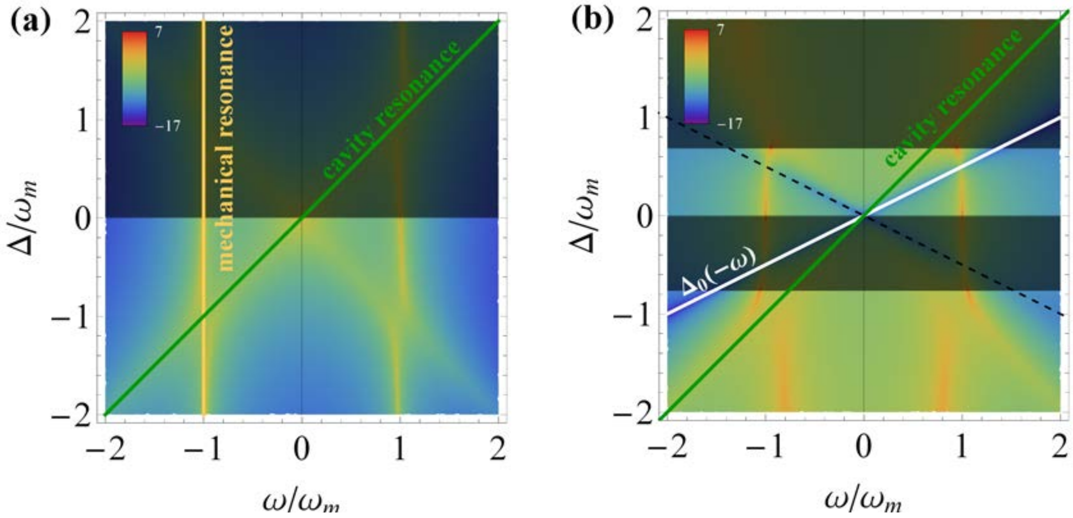

Figure 3.4.: Logarithm of the optical output spectrum $S_{dd}^{\text{out}}(\omega)$ for (a) purely dispersive coupling ($\tilde{A}\bar{a} = 0.4$ and $\tilde{B} = 0$) and (b) purely dissipative coupling ($\tilde{A} = 0$ and $\tilde{B}\bar{a} = 0.4$). Other parameters are the same as in Fig. 3.1. Dark regions indicate regions of instability. The white line indicates an exact zero of $S_{dd}^{\text{out}}(\omega)$. The dashed line indicates where the mechanical oscillator experiences dissipative cooling associated with the white line in Fig. 3.1 (a).

the covariance matrix formalism. Defining the vectors

$$\boldsymbol{u}(t) = \begin{pmatrix} \hat{d} \\ \hat{d}^\dagger \\ \hat{c} \\ \hat{c}^\dagger \end{pmatrix}, \boldsymbol{u}_{\mathbf{in}}(t) = \begin{pmatrix} \hat{\xi}_{\text{in}} \\ \hat{\xi}_{\text{in}}^\dagger \\ \hat{\eta} \\ \hat{\eta}^\dagger \end{pmatrix}, \tag{3.24}$$

the covariance matrix $\boldsymbol{V} = \langle \boldsymbol{u}(t)\boldsymbol{u}(t)^\top \rangle$ contains all possible two-operator combinations of $\hat{d}$,$\hat{d}^\dagger$,$\hat{c}$, and $\hat{c}^\dagger$. Note, that these 16 combinations are not all independent. The mean phonon number $\langle \hat{n} \rangle$ which we want to derive, is one of the entries of $\boldsymbol{V}$. We can write down the linearized equations of motion (1.15) and (1.16) as a matrix differential equation in the time-domain

$$\dot{\boldsymbol{u}}(t) = \boldsymbol{M}\boldsymbol{u}(t) - \boldsymbol{F}\boldsymbol{u}_{\mathbf{in}}(t), \tag{3.25}$$

where $\boldsymbol{M}$ and $\boldsymbol{F}$ are the matrices defined in Eqs. (3.15) and (3.16). Then, the derivative of the covariance matrix can be written as

$$\begin{aligned} \dot{\boldsymbol{V}} &= \langle \dot{\boldsymbol{u}}\boldsymbol{u}^\top \rangle + \langle \boldsymbol{u}\dot{\boldsymbol{u}}^\top \rangle = \boldsymbol{M}\langle \boldsymbol{u}\boldsymbol{u}^\top \rangle - \boldsymbol{F}\langle \boldsymbol{u}_{\mathbf{in}}\boldsymbol{u}^\top \rangle + \langle \boldsymbol{u}\boldsymbol{u}^\top \rangle \boldsymbol{M}^\top - \langle \boldsymbol{u}\boldsymbol{u}_{\mathbf{in}}{}^\top \rangle \boldsymbol{F}^\top \\ &= \boldsymbol{M}\boldsymbol{V} + \boldsymbol{V}\boldsymbol{M}^\top - \boldsymbol{F}\langle \boldsymbol{u}_{\mathbf{in}}\boldsymbol{u}^\top \rangle - \langle \boldsymbol{u}\boldsymbol{u}_{\mathbf{in}}{}^\top \rangle \boldsymbol{F}^\top. \end{aligned} \tag{3.26}$$

To calculate the expectation values appearing in the last two terms, we use the formal solution of the inhomogeneous differential equation (3.25), which is given by

$$\boldsymbol{u}(t) = e^{\boldsymbol{M}t}\boldsymbol{u}(0) - \int\limits_0^t dt' e^{\boldsymbol{M}(t-t')}\boldsymbol{F}\boldsymbol{u}_{\mathbf{in}}(t') \tag{3.27}$$

and its transpose

$$\boldsymbol{u}^\top(t) = \boldsymbol{u}(0)^\top e^{\boldsymbol{M}^\top t} - \int\limits_0^t dt' \boldsymbol{u}_{\mathbf{in}}{}^\top(t')\boldsymbol{F}^\top e^{\boldsymbol{M}^\top(t-t')}. \tag{3.28}$$

Then we find

$$\langle \boldsymbol{u}_{\mathbf{in}}(t)\boldsymbol{u}^\top(t)\rangle = \langle \boldsymbol{u}_{\mathbf{in}}(t)\boldsymbol{u}^\top(0)e^{\boldsymbol{M}^\top t}\rangle - \int\limits_0^t dt' \langle \boldsymbol{u}_{\mathbf{in}}(t)\boldsymbol{u}_{\mathbf{in}}{}^\top(t')\rangle \boldsymbol{F}^\top e^{\boldsymbol{M}^\top(t-t')}, \tag{3.29}$$

where the first term is transient and vanishes for $t \to \infty$ if we focus on stable parameter regions. The second term contains expectation values of all possible bath operator combinations. Those are given in Eq. (3.17) and lead to

$$\langle \boldsymbol{u}_{\mathbf{in}}(t)\boldsymbol{u}_{\mathbf{in}}{}^\top(t')\rangle = \begin{pmatrix} 0 & 1 & 0 & 0 \\ 0 & 0 & 0 & 0 \\ 0 & 0 & 0 & n_{\mathrm{th}}+1 \\ 0 & 0 & n_{\mathrm{nth}} & 0 \end{pmatrix} \delta(t-t'). \tag{3.30}$$

Denoting this matrix

$$\boldsymbol{N} = \begin{pmatrix} 0 & 1 & 0 & 0 \\ 0 & 0 & 0 & 0 \\ 0 & 0 & 0 & n_{\mathrm{th}}+1 \\ 0 & 0 & n_{\mathrm{nth}} & 0 \end{pmatrix}, \tag{3.31}$$

and using $t \to \infty$ we can write the expectation value as

$$\langle \boldsymbol{u}_{\mathbf{in}}(t)\boldsymbol{u}^\top(t)\rangle = -\int\limits_0^\infty dt' \boldsymbol{N}\boldsymbol{F}^\top e^{\boldsymbol{M}^\top(t-t')}\delta(t-t') = -\frac{1}{2}\boldsymbol{N}\boldsymbol{F}^\top. \tag{3.32}$$

Repeating the calculation for the expectation value from the last term in Eq. (3.26) leads to

$$\begin{aligned}\langle \boldsymbol{u}(t)\boldsymbol{u}_{\mathbf{in}}{}^\top(t)\rangle &= \langle \boldsymbol{u}(0)e^{\boldsymbol{M}t}\boldsymbol{u}_{\mathbf{in}}(t)^\top\rangle - \int\limits_0^t dt' e^{\boldsymbol{M}(t-t')}\boldsymbol{F}\langle \boldsymbol{u}_{\mathbf{in}}(t')\boldsymbol{u}_{\mathbf{in}}{}^\top(t)\rangle \\ &= -\int\limits_0^\infty dt' e^{\boldsymbol{M}(t-t')}\boldsymbol{F}\boldsymbol{N}\delta(t'-t) = -\frac{1}{2}\boldsymbol{F}\boldsymbol{N}.\end{aligned} \tag{3.33}$$

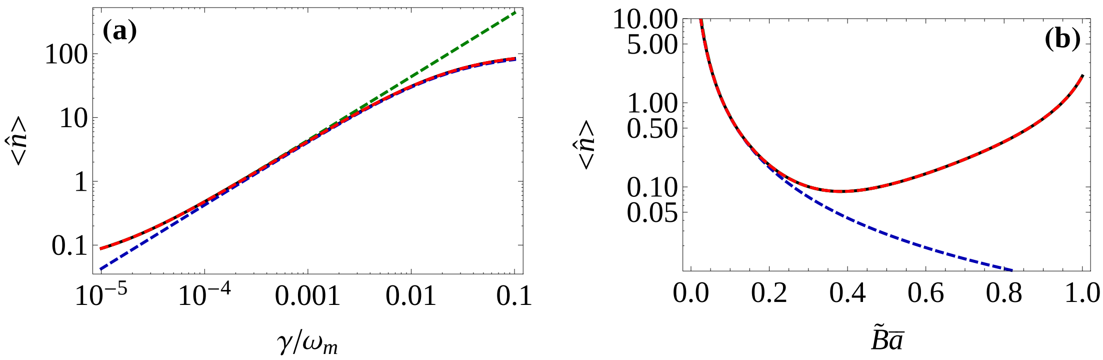

Figure 3.5.: Mean phonon number $\langle\hat{n}\rangle$ obtained from the exact solution of the covariance matrix formalism (black solid line), from the approximation Eq. (3.35) (green dashed line), from numerical integration of Eq. (3.19) (red dashed line) and $n_{\rm osc}$ from the quantum noise approach of Chapter 2 (blue dashed line). (a) shows $\langle\hat{n}\rangle$ as a function of the mechanical damping γ, (b) as a function of the effective coupling strength $\tilde{B}\bar{a}$. Parameters are $\omega_m/\kappa = 3$, $n_{\rm th} = 100$, $\Delta = \omega_m/2$, $\tilde{A} = 0$ and either $\tilde{B}\bar{a} = 0.4$ or $\omega_m/\gamma = 10^5$. In (b) the approximation Eq. (3.35) is not visible since it coincides very well with the exact and numerical solution.

Finally, substituting Eqs. (3.32) and (3.33) into the equation of motion of the covariance matrix (3.26), we find

$$\dot{\boldsymbol{V}} = \boldsymbol{M}\boldsymbol{V} + \boldsymbol{V}\boldsymbol{M}^\top + \frac{1}{2}\boldsymbol{F}\boldsymbol{N}\boldsymbol{F}^\top + \frac{1}{2}\boldsymbol{F}\boldsymbol{N}\boldsymbol{F}^\top = \boldsymbol{M}\boldsymbol{V} + \boldsymbol{V}\boldsymbol{M}^\top + \boldsymbol{D}, \tag{3.34}$$

where $\boldsymbol{D} = \boldsymbol{F}\boldsymbol{N}\boldsymbol{F}^\top$. The steady-state solution, $\dot{\boldsymbol{V}} = 0$, of this equation can be calculated exactly, e.g. using Mathematica. However, it means to solve a linear system of 16 equations, having 16 variables, although not all of them are independent. The result is very cumbersome, thus we focus on purely dissipative coupling, i.e. $\tilde{A} = 0$, and the entry of the covariance matrix $\boldsymbol{V}$ that gives the mean phonon number $\langle\hat{n}\rangle$. Furthermore, we neglect all terms proportional to the mechanical damping γ and keep only terms containing the product $\gamma n_{\rm th}$. Then, the result is given by

$$\begin{aligned}\langle\hat{n}\rangle = \frac{1}{z}\Big\{&\tilde{B}^4\Delta[-n_{\rm th}\gamma\Delta\left(4\Delta^2-3\kappa^2\right)^2\left(4\Delta^2+\kappa^2\right)+8\Delta^2\kappa\left(-16\Delta^4+8\Delta^2\kappa^2+3\kappa^4\right)\omega_m\\ &-16\Delta\kappa\left(16\Delta^4+4\Delta^2(n_{\rm th}\gamma-4\kappa)\kappa+\kappa^3(n_{\rm th}\gamma+3\kappa)\right)\omega_m^2+2\kappa\left(16\Delta^4-104\Delta^2\kappa^2+5\kappa^4\right)\omega_m^3\\ &+64\Delta\left(-2\kappa^3+n_{\rm th}\gamma\left(4\Delta^2-3\kappa^2\right)\right)\omega_m^4+64\kappa^3\omega_m^5]\\ &-4n_{\rm th}\gamma\left(4\Delta^2+\kappa^2\right)\left[\kappa^2+4(\Delta-\omega_m)^2\right]\omega_m^2\left[\kappa^2+4(\Delta+\omega_m)^2\right]\\ &-2\tilde{B}^6\Delta^2\left(4\Delta^2-3\kappa^2\right)\omega_m\left[2n_{\rm th}\gamma\Delta\left(4\Delta^2+\kappa^2\right)+\kappa\omega_m\left(4\Delta^2+\kappa^2+16\Delta\omega_m-8\omega_m^2\right)\right]\\ &+4\tilde{B}^2\omega_m[n_{\rm th}\gamma\Delta\left(\left(4\Delta^2+\kappa^2\right)^2\left(-4\Delta^2+3\kappa^2\right)+8\left(16\Delta^4-16\Delta^2\kappa^2+3\kappa^4\right)\omega_m^2+64\kappa^2\omega_m^4\right)\\ &-\kappa\left(4\Delta^2+\kappa^2\right)\omega_m(-2\Delta+\omega_m)^2\left(\kappa^2+4(\Delta+\omega_m)^2\right)]\Big\}\,,\end{aligned} \tag{3.35}$$

where

$$z = 32\tilde{B}^2\Delta\kappa\omega_m^2\left[\tilde{B}^2\left(4\Delta^3-3\Delta\kappa^2\right)+\left(4\Delta^2+\kappa^2\right)\omega_m\right]\left(4\Delta^2-\kappa^2+2\tilde{B}^2\Delta\omega_m-2\omega_m^2\right). \tag{3.36}$$

Unfortunately, this result still gives not much insight, but it coincides well with the result obtained by numerical integration of the mechanical spectrum $S_{cc}(\omega)$ and can be evaluated faster. Furthermore, Eq. (3.35) could be used to numerically optimize the mean phonon number for certain parameters, e.g. the coupling strength $\tilde{B}\bar{a}$, the sideband parameter ω_m/κ or the detuning Δ.

Figure 3.5 (a) illustrates that the exact solution and the numerical integration of Eq. (3.19) match very well. As expected, the approximation Eq. (3.35) is consistent with the exact solution for sufficiently small mechanical damping γ. The phonon number $n_{\rm osc}$ calculated from the quantum noise approach applied in Chapter 2 differs from the exact solution due to the used strong coupling, however it captures the behaviour for large γ, i.e. small mechanical quality factors.

Figure 3.5 (b) shows the most striking difference between the weak-coupling solution and the strong-coupling results: Whereas the quantum noise approach predicts unlimited improvement of the cooling result with increasing coupling strength, the exact strong-coupling calculation reveals that the phonon number increases again if the coupling becomes too strong. An exact expression for this cooling limit remains to be derived.

4. Optomechanically induced transparency (OMIT)

In this chapter we will investigate the response of the optomechanically-coupled system to a weak probe field, and show that purely dissipative coupling, i.e. $\tilde{A} = 0$, leads to optomechanically-induced transparency. This is also a convenient way to observe normal-mode splitting (NMS). We compare our findings to the purely dispersive case and give an appropriate approximation that holds in the general case of dispersive and dissipative coupling, i.e. $\tilde{A} \neq 0$ and $\tilde{B} \neq 0$, in the resolved-sideband regime.

The probe field of frequency ω_p is assumed to be weak compared to the drive field, i.e. its optomechanical coupling can be neglected. Thus it is sufficient to account for the probe laser by changing the optical input mode $\hat{\xi}_{\text{in}}(\omega)$ in an appropriate way and neglecting additional coupling terms. In the preceding chapters, the operator $\hat{\xi}_{\text{in}}$ denoted vacuum fluctuations only, now it contains the probe field such that $\hat{\xi}_{\text{in}}(t) = \hat{\xi}_{\text{vac}}(t) + \bar{d}_{\text{probe}} e^{-i\delta t}$ with $\langle \hat{\xi}_{\text{in}}(t) \rangle = \bar{d}_{\text{probe}} e^{-i\delta t}$. Here $\hat{\xi}_{\text{vac}}$ describes the vacuum fluctuations of the optical bath, $\delta = \omega_p - \omega_d$ denotes the detuning between probe and drive laser and $\bar{d}_{\text{probe}}$ is the amplitude of the probe laser.

We investigate the response to the probe field by evaluating the expectation value of the optical output mode (3.13). Since $\langle \hat{\eta} \rangle = \langle \hat{\eta}^\dagger \rangle = 0$, the result is of the form

$$\langle \hat{\xi}_{\text{out}}(t) \rangle = \int_{-\infty}^{+\infty} \frac{d\omega}{2\pi} \langle \hat{\xi}_{\text{out}}(\omega) \rangle e^{-i\omega t} = A^- e^{-i\delta t} + A^+ e^{i\delta t}. \tag{4.1}$$

Recall that all calculations are done in a frame rotating with $-\omega_d$, thus the optical output contains terms rotating at three frequencies: $-\omega_d$ (drive frequency), $-\delta - \omega_d = -\omega_p$ (anti-Stokes field) and $\delta - \omega_d = \omega_p - 2\omega_d$ (Stokes field). The contribution at the drive frequency is not contained in Eq. (4.1) since we treated the coherent part of the drive separately with Eqs. (1.11) and (1.12), i.e. $\hat{\xi}_{\text{out}}$ only describes the fluctuations around the strong drive field. A^- and A^+ are the complex amplitudes of the anti-Stokes and Stokes field and are given by

$$A^- = \left[1 - \kappa \chi_c(\delta) + 2i\kappa\omega_m \frac{|\bar{a}|^2 \alpha(\delta)^2}{\mathcal{N}(\delta)} \right] \bar{d}_{\text{probe}}, \tag{4.2}$$

$$A^+ = -2i\kappa\omega_m \frac{\bar{a}^2 \alpha^*(\delta) \alpha(-\delta)}{\mathcal{N}(-\delta)} \bar{d}^*_{\text{probe}}. \tag{4.3}$$

The anti-Stokes field rotates with the probe frequency $-\omega_p$, thus A^- is the amplitude of the original probe field modified due to interference with anti-Stokes scattered light ($\delta > 0$) from the drive field. Furthermore, A^+ is the amplitude of the output field

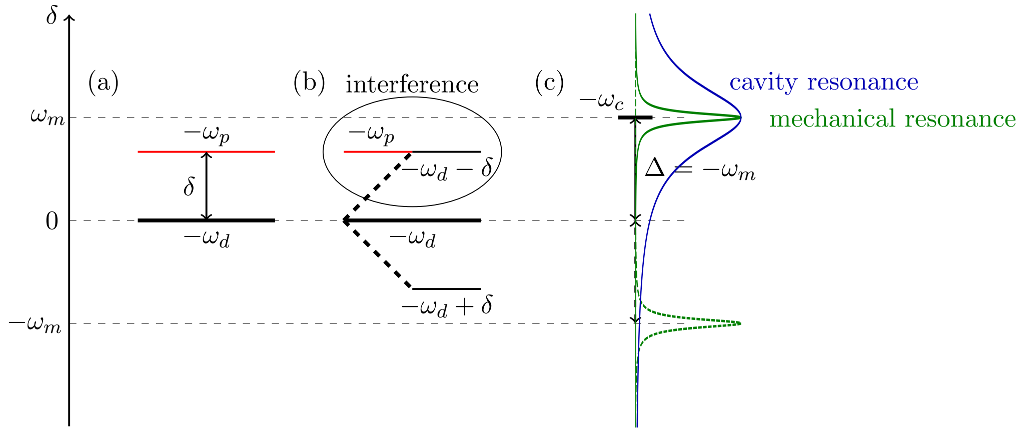

Figure 4.1.: Illustration of the relevant frequencies involved in OMIT, in the frame of the drive ω_d. (a) shows the frequencies contained in the full input mode, i.e. the frequencies injected into the optomechanical system by the optical drive ω_d and the probe laser ω_p. (b) illustrates the frequencies contained in the full output-mode. The total contribution at $-\omega_p = -\omega_d - \delta$ results from the interference of the injected probe field and a field at the same frequency created through the optomechanical coupling of the drive field. This is the origin of the OMIT signal. The weight of the frequencies created by the optomechanical coupling strongly depends on whether the resonance conditions of the optics and mechanics, indicated in (c), are met or not.

component rotating at a frequency $\omega_p - 2\omega_d$ that is created by the optomechanical coupling, i.e. Stokes scattering ($\delta > 0$) of drive photons. Figure 4.1 illustrates the involved frequencies.

Focusing on the anti-Stokes contribution at $\Delta = -\omega_m$ where NMS appears in the mechanical spectrum $S_{cc}(\omega)$, Eq. (4.2) consists of three contributions to the amplitude A^-: The constant first term accounts for the initial probe field. The second term represents the influence of the uncoupled cavity. Finally, the third term is nonzero only for nonzero coupling and contains the influence of both dispersive and dissipative coupling.

Using homodyne detection, different quadratures of the anti-Stokes field can be investigated experimentally. Figure 4.2 shows the real part of the anti-Stokes amplitude, $\mathrm{Re}[A^-]$. In absence of optomechanical coupling the cavity leads to a Lorentzian-shaped dip of width κ associated with the second term in Eq. (4.2). For nonzero coupling the third term in Eq. (4.2) modifies the amplitude due to scattering processes from the drive to this frequency. These processes are suppressed away from the mechanical resonance, thus striking modifications occur only for $\delta \approx \pm\omega_m$. There, an upper or lower sideband

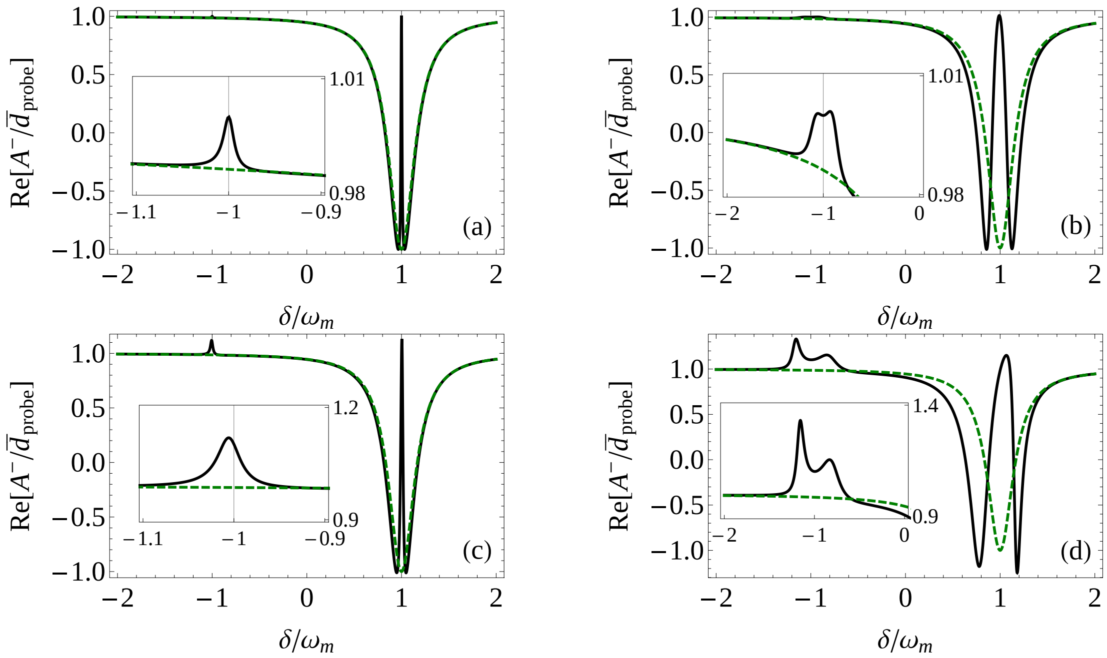

Figure 4.2.: The real part $\mathrm{Re}[A^-/\bar{d}_{\text{probe}}]$ of the response at the probe frequency $-\omega_p$ as a function of the detuning between probe and drive field δ for $\Delta = -\omega_m$. (a) and (b) show the case of purely dispersive coupling with $\tilde{A}\bar{a} = 0.1$ and $\tilde{A}\bar{a} = 0.4$. (c) and (d) show purely dissipative coupling with $\tilde{B}\bar{a} = 0.1$ and $\tilde{B}\bar{a} = 0.4$. Other parameters are the same as in Fig. 3.1. The green dashed line shows the result in absence of coupling ($\tilde{A} = \tilde{B} = 0$). The insets show a magnification around $\delta = -\omega_m$.

$-\omega_d \pm \omega_m$ is created and its frequency coincides with the probe frequency $-\omega_p$, which gives rise to interference effects [14, 15].

At $\delta = -\omega_m$, scattering from the drive laser is not suppressed by the mechanical response, but in the resolved sideband regime, i.e. $\omega_m \gg \kappa$, this process is highly off-resonant with respect to the cavity frequency. Thus, the effect at this frequency is small. As shown in the insets of Fig. 4.2, dissipative coupling leads to a larger contribution at detuning $\delta \approx -\omega_m$ than purely dispersive coupling. This originates from the direct interaction between optical bath and mechanical oscillator: It gives rise to a constant contribution to $\alpha(\delta)^2$ in Eq. (4.2), i.e. a term not filtered by the cavity response function.

In contrast, if $\delta = +\omega_m$ and $\Delta = -\omega_m$, the probe frequency ω_p coincides with the cavity resonance ω_c, giving rise to more prominent effects. The optomechanical coupling leads to a narrow peak enclosed by a broad dip that appears also in absence of coupling. For small coupling as shown in Figs. 4.2 (a) and (c), the width of this peak is given by the width of the mechanical resonance. The mechanical linewidth, in turn, is given by the intrinsic damping γ and broadened with increasing coupling strength due to the additional optical damping γ_{opt}. In the case of sufficiently strong coupling, see Figs. 4.2

(b) and (d), the two modes are separated by a peak that has a width comparable to or larger than the width of each of the modes. The splitting increases for stronger coupling.

This general behaviour is shared by dissipatively and dispersively coupled systems, but there are small differences: First, the width of the splitting in the case of purely dissipative and purely dispersive coupling depends differently on the respective coupling strength. Second, there is an increasing asymmetry between the two modes in the case of dissipative coupling, whereas purely dispersive coupling leads to a splitting into two anti-peaks that remain similar over a larger range of coupling strengths.

In analogy to the treatment of purely dispersive coupling [14], we assume that only anti-Stokes scattering occurs. This can be described by simplified equations of motion where we neglect coupling to $\hat{d}^\dagger$ and $\hat{c}^\dagger$ in Eqs. (1.15) and (1.16), for details see Appendix B.5. As a result $\langle\hat{\xi}_{\text{out}}(t)\rangle$ is still of the form of Eq. (4.1), but with new coefficients $A^+_{\text{approx}} = 0$ and

$$A^-_{\text{approx}} = \left[1 - \kappa\chi_c(\delta) - \kappa\frac{|\bar{a}|^2\alpha(\delta)^2}{\chi_m^{-1}(\delta) + i\tilde{\Sigma}(\delta)}\right]\bar{d}_{\text{probe}} \tag{4.4}$$

where $\tilde{\Sigma}(\omega) = \tilde{\Sigma}_{\tilde{A}}(\omega) + \tilde{\Sigma}_{\tilde{B}}(\omega) + \tilde{\Sigma}_{\tilde{A}\tilde{B}}(\omega)$. Here, $\tilde{\Sigma}_{\tilde{A}}(\omega) = -i(\tilde{A}\kappa|\bar{a}|)^2\chi_c(\omega)$, $\tilde{\Sigma}_{\tilde{B}}(\omega) = i(\tilde{B}/2)^2\,|\bar{a}|^2\,\chi_c(\omega)(i\Delta + \kappa/2)^2$, and $\tilde{\Sigma}_{\tilde{A}\tilde{B}}(\omega) = \tilde{B}\tilde{A}\kappa\,|\bar{a}|^2\,\chi_c(\omega)(i\Delta + \kappa/2)$ denote only the parts of the originally defined self-energies with weight at $\delta \approx +\omega_m$. In the case of $\tilde{B} = 0$ the approximation is the same as in Ref. [14]. For both dispersive and dissipative coupling, the approximation is valid in the resolved-sideband regime, e.g. it does not reproduce the feature at $\delta = -\omega_m$ which becomes more important if ω_m is of the order of κ or the coupling becomes too strong.

Conclusion and outlook

In this thesis we have presented a detailed study of optomechanical systems featuring both dissipative and dispersive coupling. Dissipative coupling originates from a displacement-dependent cavity linewidth, whereas dispersive coupling originates from a displacement-dependent cavity resonance frequency. We have pointed out new features due to dissipative coupling as well as discussed differences of shared effects of dispersively and dissipatively coupled systems. A quantum noise approach and the exact solution to the linearized equations of motion have been used to investigate weak- and strong-coupling properties, respectively.

For weak coupling we have calculated the optical damping and the optically-induced frequency shift. Surprisingly, there are two regions leading to cooling and two regions leading to amplification. This is a consequence of the Fano line shape in the force spectrum which is absent for purely dispersive coupling. Notably, the weak-coupling approach predicts unlimited cooling independent of the sideband parameter [16].

In the strong-coupling regime we have first derived the exact solution to the linearized equations of motion in the general case of both dispersive and dissipative coupling. Then, we calculated and discussed the mechanical and the optical spectra. Similar to purely dispersive coupling, normal-mode splitting appears for sufficiently strong coupling. Nonzero dissipative coupling additionally leads to a striking feature which originates from quantum noise interference. Since the exact strong-coupling calculations shows that cooling of the mechanical motion is limited, we have applied the covariance matrix formalism to derive an analytic expression for the final mean phonon number. Finally, we have found that purely dissipative coupling can lead to optomechanically-induced transparency which will be an experimentally convenient way to observe normal-mode splitting.

In contrast to dispersively coupled systems, various properties of dissipatively coupled systems remain yet unknown or to be explored in more detail. Although it was realized from the beginning that dissipative cooling at the optimal detuning is not unlimited, as indicated by a weak-coupling approach [16], an expression for the strong-coupling limit has yet to be determined. Furthermore, properties of the optical output field, e.g. squeezing and statistical behaviour like bunching or anti-bunching remain to be investigated. Moreover, optomechanical systems including both types of coupling could lead to interesting new features if the relative sign of the coupling strengths is considered. Besides, also the classical equations of motion of dissipatively coupled optomechanical systems still offer new options. The static bistability and the exact stability conditions of the mean-field treatment need to be investigated in more detail.

Acknowledgements

I want to acknowledge the kind support of my supervisor Prof. Dr. Christoph Bruder and especially the numerous interesting and helpful discussions with Dr. Andreas Nunnenkamp. I am very grateful for their advice and invested time.
Furthermore, I want to acknowledge helpful discussions on the topic of the covariance matrix formalism with Samuel Aldana.

Appendix

A. List of variables

Variable	Meaning	First appearance/definition
$\tilde{A}$	dimensionless *dispersive* coupling strength	page 6
$\tilde{B}$	dimensionless *dissipative* coupling strength	page 6
$\hat{a}^\dagger$,$\hat{a}$	bosonic creation and annihilation operators of the optical mode inside the cavity	page 7
$\hat{d}^\dagger$,$\hat{d}$	bosonic creation and annihilation operators of the fluctuations of the optical mode inside the cavity	page 8
$\hat{b}^\dagger$,$\hat{b}$	bosonic creation and annihilation operators of the mechanical mode	page 7
$\hat{c}^\dagger$,$\hat{c}$	bosonic creation and annihilation operators of the fluctuations of the mechanical mode	page 8
$\hat{x}_\mathrm{m}$	operator of the mechanical displacement from its equilibrium position	page 6
$\hat{x}$	operator of the mechanical displacement relative to its steady-state position $\bar{x}$	page 8
$\bar{x}$	steady-state position of the mechanical oscillator; static shift from the equilibrium position due to optomechanical coupling	page 8
$\hat{n}$	phonon number operator	page 21
$\hat{b}_q^\dagger$,$\hat{b}_q$	operators of the optical bath mode q	page 7
$\hat{\eta}^\dagger$,$\hat{\eta}$	fluctuations of the mechanical input mode; a sum of mechanical bath operators	page 8/Eq. (3.17)
$\hat{a}_\mathrm{in}^\dagger$,$\hat{a}_\mathrm{in}$	optical input mode	page 7/Eq. (B.4)
$\bar{a}_\mathrm{in}$	coherent part of the optical input mode	page 8
$\hat{\xi}_\mathrm{in}^\dagger$,$\hat{\xi}_\mathrm{in}$	fluctuations of the optical input mode; a sum of optical bath operators; used with a slightly different definition in Chapter 4 (definition on page 31)	page 8/Eq. (3.17)
$\hat{a}_\mathrm{out}^\dagger$,$\hat{a}_\mathrm{out}$	optical output mode	page 7/Eq. (B.5)
$\bar{a}_\mathrm{out}$	coherent part of the optical output mode	page 19

Variable	Meaning	First appearance/definition
$\hat{\xi}^\dagger_{\mathrm{out}}$,$\hat{\xi}_{\mathrm{out}}$	fluctuations of the optical output mode, a sum of optical bath operators	page 19
$\hat{\xi}^\dagger_{\mathrm{vac}}$,$\hat{\xi}_{\mathrm{vac}}$	vacuum fluctuations of the optical input mode; a sum of optical bath operators; used only in Chapter 4	page 31
$\hat{F}$	operator of the optomechanical force	page 12/Eq. (2.1)
$\bar{a}$	intra-cavity amplitude	page 8
$\bar{b}$	coherent part of the mechanical mode	page 8
Ω	strength of the coherent laser drive	page 8
$\bar{d}_{\mathrm{probe}}$	amplitude of the probe laser	page 31
κ	cavity linewidth	page 6
γ	damping rate of the mechanical oscillator	page 7
γ_{opt}	optical damping due to the optomechanical coupling	page 14
γ_{tot}	total damping of the mechanical oscillator (includes intrinsic and optical damping)	page 14
ω_c	cavity resonance frequency	page 6
ω_d	frequency of the drive laser providing a coherent drive	page 8
ω_m	resonance frequency of the mechanical oscillator	page 6
ω_p	frequency of the probe laser	page 31
ω_q	frequency of the optical bath mode q	page 7
$\delta\omega_m$	optically-induced frequency shift	page 14 and Appendix B.4
n_{th}	thermal equilibrium phonon number	page 8
n_{opt}	minimal phonon number caused by coupling the mechanics to the optics only	page 14
n_{osc}	steady-state mean phonon number (in presence of a mechanical bath and the optomechanical coupling)	page 14
$\Gamma_{n\to n+1}, \Gamma_{n\to n-1}$	transition rates between neighbouring phonon number states	page 12
$\Gamma_\uparrow(\Gamma_\downarrow)$	amplification (cooling) rate	page 12
$\hat{\mathscr{H}}$	Hamiltonian of the full system	page 7/Eq. (1.2)
$\hat{\mathscr{H}}_2$	Hamiltonian of the full system using a second order expansion of κ and ω_c in the displacement x	page 43/Eq. (B.12)
$\hat{H}$	simplified, non-hermitian Hamiltonian to describe normal-mode splitting	page 23/Eq. (3.20)
$\hat{H}_\kappa$	Hamiltonian of the optical bath	page 7
$\hat{H}_\gamma$	Hamiltonian of the mechanical bath	page 7
Δ	detuning between drive laser and cavity resonance	page 8

Variable	Meaning	First appearance/definition
$\Delta_0(\omega)$	function that determines the relation between Δ and ω such that $S_{FF}(\omega) = 0$	page 14/Eq. (2.4)
Δ_{opt}	optimal detuning in presence of dissipative coupling; implies $S_{FF}(-\omega_m) = 0$	page 14/Eq. (2.5)
δ	detuning between drive and probe laser	page 31
$\chi_c(\omega)$	cavity response function	page 12
$\chi_m(\omega)$	mechanical response function	page 18
$\Sigma(\omega)$	optomechanical self-energy	page 18/Eq. (3.6)
$\Sigma_{\tilde{X}}(\omega)$	optomechanical self-energy due to coupling $\tilde{X}$	page 18/Eq. (3.7)
$\tilde{\Sigma}_{\tilde{X}}(\omega)$	approximate optomechanical self-energy due to coupling $\tilde{X}$, used in Chapter 4 only	page 34/Eq. (B.49)
$\alpha(\omega)$	auxiliary function, also defined for different couplings $\tilde{X}$ as $\alpha_{\tilde{X}}(\omega)$	page 18/Eqs. (3.6),(3.8)
$\mathscr{N}(\omega)$	auxiliary function	page 19
$\sigma_{\text{th}}(\omega)$	auxiliary function	page 21
$\sigma_{\text{opt}}(\omega)$	auxiliary function	page 21
$S_{FF}(\omega)$	weak-coupling force spectrum	page 13/Eq. (2.3)
$S_{cc}(\omega)$	mechanical spectrum	21/Eq. (3.19)
$S_{xx}(\omega)$	displacement spectrum	page 25
$S_{dd}(\omega)$	cavity spectrum	page 25/Eq. (3.22)
$S_{dd}^{\text{out}}(\omega)$	optical output spectrum	page 25/Eq. (3.23)
$A^-(A^+)$	amplitude of the negative (positive) frequency component of the output mode	page 31/Eq. (4.2) and (4.3)
$A^+_{\text{approx}}(A^-_{\text{approx}})$	approximate amplitude of the positive (negative) frequency component of the output mode	page 34/Eq. (4.4)
x_0	zero point fluctuation of the mechanical oscillator	page 6
m	mass of the mechanical oscillator	page 6
ρ	density of states of the optical bath	page 7
T	temperature associated with the thermal equilibrium phonon number n_{th}	page 8
k_B	Boltzmann's constant	page 8
t_0	initial time, before the laser drive reaches the cavity	page 41
t_1	final time, after the light of the laser drive has left the cavity	page 41
$\hat{\mathfrak{a}}$	operator defined for shorter notation only	page 41
p	an arbitrary pole	page 50
$\nu(p)$	winding number of the integration path around pole p	page 50
$f(\omega)$	an arbitrary function	page 50
$g(\omega)$	the numerator of the arbitrary function $f(\omega)$	page 50
$h(\omega)$	the denominator of the arbitrary function $f(\omega)$	page 50

Variable	Meaning	First appearance/definition
r_{0a}, r_{1a}, r_{2a}	residues corresponding to the poles in Fig. B.5 (a)	page 51/Eq. (B.39)
r_{0b}, r_{1b}, r_{2b}	residues corresponding to the poles in Fig. B.5 (b)	page 51/Eq. (B.39)
α	the complete, closed integration path in Fig. B.5	page 50
$\beta(t)$	parametrization of the arc that closes the integration path in Fig. B.5	page 50 and 51
$\boldsymbol{u}(t)$	vector containing the optical and mechanical operators $\hat{d}$, $\hat{d}^\dagger$, $\hat{c}$, $\hat{c}^\dagger$	page 27/Eq. (3.24)
$\boldsymbol{u}_{\mathbf{in}}(t)$	vector containing the optical and mechanical input modes $\hat{\xi}_{\mathrm{in}}$, $\hat{\xi}_{\mathrm{in}}^\dagger$, $\hat{\eta}$, $\hat{\eta}^\dagger$	page 27/Eq. (3.24)
$\boldsymbol{M}$	matrix containing the coefficients of the optical and mechanical modes	page 20/Eq. (3.15)
$\boldsymbol{F}$	fluctuation matrix	page 20/Eq. (3.16)
$\boldsymbol{V}$	covariance matrix	page 27
$\boldsymbol{N}$	matrix containing the expectation values of the input modes	page 28/Eq. (3.31)
$\boldsymbol{D}$	matrix defined as a combination of the matrices $\boldsymbol{N}$ and $\boldsymbol{F}$	page 29
D	discriminant of a third order polynomial	page 45
z_B	'effective' dissipative coupling strength; depends on $\tilde{B}$ and properties of the mechanical oscillator	page 44
z_A	'effective' dispersive coupling strength; depends on $\tilde{A}$ and properties of the mechanical oscillator	page 46
z_{AB}	mixed coupling term, containing $\tilde{A}$, $\tilde{B}$ and properties of the mechanical oscillator	page 46
z	auxiliary variable	page 30/Eq. (3.36)

B. Further calculations

B.1. Input-output relation including dissipative coupling

The input-output formalism [21,22] is a useful tool to describe the coupling of a system to external heat baths in terms of input and output modes. In our case, it allows to replace the bath-operators $\hat{b}_q$, e.g. appearing in the Heisenberg equation of motion of the cavity mode $\hat{a}$, by quantities with known expectation values. Since dissipative coupling introduces an additional coupling of $\hat{x}_m$ and $\hat{b}_q$ ($\hat{b}_q^\dagger$), we have to modify the input-output equation used for dispersive coupling. In this section we will not repeat the complete derivation (for this see e.g. [22,23]), but only point out the modifications that need to be applied to account for both types of coupling.

The equation of motion for the bath operators in presence of dispersive and dissipative coupling is given by

$$\begin{aligned}
\dot{\hat{b}}_q &= i\left[\hat{\mathscr{H}}, \hat{b}_q\right] \\
&= i\left[\omega_q \hat{b}_q^\dagger \hat{b}_q, \hat{b}_q\right] + \sqrt{\frac{\kappa}{2\pi\rho}}\left(1 + \frac{\tilde{B}}{2}\frac{\hat{x}_m}{x_0}\right)\underbrace{\sum_{q'}\left[\hat{a}^\dagger \hat{b}_{q'} - \hat{b}_{q'}^\dagger \hat{a}, \hat{b}_q\right]}_{=\hat{a}} \\
&= -i\omega \hat{b}_q + \sqrt{\frac{\kappa}{2\pi\rho}}\left(1 + \frac{\tilde{B}}{2}\frac{\hat{x}_m}{x_0}\right)\hat{a}.
\end{aligned} \tag{B.1}$$

Dissipative coupling leads to a new term proportional to the coupling strength $\tilde{B}$ and introduces a non-linearity. However, for the purpose of the derivation, we can define $\hat{\mathfrak{a}}(t) = \left(1 + \frac{\tilde{B}}{2}\frac{\hat{x}_m(t)}{x_0}\right)\hat{a}(t)$ and proceed as it is done for the purely dispersive case. The solution of the differential equation (B.1) can be expressed depending on some initial time $t_0 < t$ in the distant past

$$\hat{b}_q(t) = e^{-i\omega_q(t-t_0)}\hat{b}_q(t_0) + \sqrt{\frac{\kappa}{2\pi\rho}}\int_{t_0}^{t} d\tau e^{-i\omega_q(t-\tau)}\hat{\mathfrak{a}}(\tau) \tag{B.2}$$

or, formally equal, depending on a time $t_1 > t$ in the distant future,

$$\hat{b}_q(t) = e^{-i\omega_q(t-t_1)}\hat{b}_q(t_1) - \sqrt{\frac{\kappa}{2\pi\rho}}\int_{t}^{t_1} d\tau e^{-i\omega_q(t-\tau)}\hat{\mathfrak{a}}(\tau). \tag{B.3}$$

Since Eq. (B.2) and Eq. (B.3) have the same structure as in the case of purely dispersive coupling, we make use of the Markov approximation and follow the derivation for dispersive coupling, [22,23]. The input (output) mode is not affected by dissipative coupling because its definition depends on the first term of Eq. (B.2) (Eq. (B.3)) only. Thus, we find

$$\hat{a}_{\text{in}} = \sqrt{\frac{\kappa}{2\pi\rho}} \sum_q e^{-i\omega_q(t-t_0)} \hat{b}_q(t_0), \tag{B.4}$$

and

$$\hat{a}_{\text{out}} = \sqrt{\frac{\kappa}{2\pi\rho}} \sum_q e^{-i\omega_q(t-t_1)} \hat{b}_q(t_1). \tag{B.5}$$

Furthermore, Eqs. (B.2) and (B.4) lead to

$$\begin{aligned} \sqrt{\frac{\kappa}{2\pi\rho}} \sum_q \hat{b}_q &= \sqrt{\kappa}\hat{a}_{\text{in}} + \frac{\kappa}{2}\hat{\mathfrak{a}} \\ &= \sqrt{\kappa}\hat{a}_{\text{in}} + \frac{\kappa}{2}\hat{a} + \frac{\kappa}{2}\frac{\tilde{B}}{2}\frac{\hat{x}_m}{x_0}\hat{a}, \end{aligned} \tag{B.6}$$

cf. Eq. (1.3), whereas using Eqs. (B.3) and (B.5) instead leads to

$$\begin{aligned} \sqrt{\frac{\kappa}{2\pi\rho}} \sum_q \hat{b}_q &= \sqrt{\kappa}\hat{a}_{\text{out}} - \frac{\kappa}{2}\hat{\mathfrak{a}} \\ &= \sqrt{\kappa}\hat{a}_{\text{out}} - \frac{\kappa}{2}\hat{a} - \frac{\kappa}{2}\frac{\tilde{B}}{2}\frac{\hat{x}_m}{x_0}\hat{a}. \end{aligned} \tag{B.7}$$

The final the input-output relation is obtained by equating Eq. (B.6) and Eq. (B.7),

$$\sqrt{\kappa}\hat{a}_{\text{in}} + \frac{\kappa}{2}\hat{a} + \frac{\kappa}{2}\frac{\tilde{B}}{2}\frac{\hat{x}_m}{x_0}\hat{a} = \sqrt{\kappa}\hat{a}_{\text{out}} - \frac{\kappa}{2}\hat{a} - \frac{\kappa}{2}\frac{\tilde{B}}{2}\frac{\hat{x}_m}{x_0}\hat{a}. \tag{B.8}$$

It follows

$$\hat{a}_{\text{in}} - \hat{a}_{\text{out}} = -\sqrt{\kappa}\hat{a} - \frac{\sqrt{\kappa}\tilde{B}}{2x_0}\hat{x}_m\hat{a}, \tag{B.9}$$

which is Eq. (1.4) given in Section 1.1.

B.2. Second-order coupling

In Eq. (1.1) we assumed a weak dependence of the cavity resonance frequency ω_c and the linewidth κ on the mechanical displacement, thus only terms up to first order in $\hat{x}_m$ were considered to achieve the Hamiltonian (1.2). Nevertheless, a quadratic term appears in the equation of motion (1.6). In this section we show that, taking all second order terms into account, this term drops out and indeed has no influence on the optomechanical system. Moreover it turns out that, if second order coupling with respect to $\hat{x}_m$ is considered, another term has to be taken into account instead. To derive this, we expand both ω_c and κ up to second order with respect to the mechanical displacement $\hat{x}_m$,

$$\begin{aligned} \omega_c(\hat{x}_m) &\approx \omega_c(0) + \left.\frac{d\omega_c(x)}{dx}\right|_{x=0} \hat{x}_m + \frac{1}{2}\left.\frac{d^2\omega_c(x)}{dx^2}\right|_{x=0} \hat{x}_m^2 \\ &= \omega_c - \tilde{A}\kappa\frac{\hat{x}_m}{x_0} - \frac{1}{2}\left(\frac{\partial \tilde{A}}{\partial x}\right)\frac{\kappa}{x_0}\hat{x}_m^2 \end{aligned} \tag{B.10}$$

and

$$\begin{aligned}\sqrt{\kappa(\hat{x})} &\approx \sqrt{\kappa(0)} + \left.\frac{d\sqrt{\kappa(x)}}{dx}\right|_{x=0} \hat{x}_m + \frac{1}{2}\left.\frac{d^2\sqrt{\kappa(\hat{x})}}{dx^2}\right|_{x=0} \hat{x}_m^2 \\ &= \sqrt{\kappa}\left[1 + \frac{\tilde{B}}{2}\frac{\hat{x}_m}{x_0} - \frac{1}{2}\left(\frac{\tilde{B}}{2}\right)^2 \frac{\hat{x}_m^2}{x_0^2} + \frac{1}{4}\left(\frac{\partial \tilde{B}}{\partial x}\right)\frac{\kappa}{x_0}\hat{x}_m^2\right]\end{aligned} \tag{B.11}$$

where we identified the dispersive ($\tilde{A}$) and dissipative coupling strength ($\tilde{B}$). Assuming that these coupling strengths itself do not explicitly depend on the displacement, i.e. $\partial\tilde{A}/\partial x = \partial\tilde{B}/\partial x = 0$, the full second-order Hamiltonian is given by

$$\begin{aligned}\hat{\mathscr{H}}_2 = &\left(\omega_c - \tilde{A}\kappa\frac{\hat{x}_m}{x_0}\right)\hat{a}^\dagger\hat{a} - i\sqrt{\frac{\kappa}{2\pi\rho}}\left[1 + \frac{\tilde{B}}{2}\frac{\hat{x}_m}{x_0} - \frac{1}{2}\left(\frac{\tilde{B}}{2}\right)^2\frac{\hat{x}_m^2}{x_0^2}\right]\sum_q\left(\hat{a}^\dagger\hat{b}_q - \hat{b}_q^\dagger\hat{a}\right) \\ &+ \omega_m\hat{b}^\dagger\hat{b} + \omega_q\hat{b}_q^\dagger\hat{b}_q + \hat{H}_\gamma.\end{aligned} \tag{B.12}$$

This Hamiltonian, compared to the first order Hamiltonian Eq. (1.2), contains an additional term that couples $\hat{x}_m^2$ to the optical bath modes $\hat{b}_q$. Thus, input-output theory is affected and has to be modified. The Heisenberg equation of motion for the bath modes is given by

$$\dot{\hat{b}}_q = i\left[\hat{\mathscr{H}}_2, \hat{b}_q\right] = -i\omega\hat{b}_q + \sqrt{\frac{\kappa}{2\pi\rho}}\left(1 + \frac{\tilde{B}}{2}\frac{\hat{x}_m}{x_0}\right)\hat{a} - \sqrt{\frac{\kappa}{2\pi\rho}}\frac{1}{2}\left(\frac{\tilde{B}}{2}\right)^2\frac{\hat{x}_m^2}{x_0^2}, \tag{B.13}$$

which contains a new quadratic term compared to Eq. (B.1). However, the input-output formalism can still be derived completely analogous to the case of purely dispersive, or first order dissipative coupling, cf. Appendix B.1. We find

$$\sqrt{\frac{\kappa}{2\pi\rho}}\sum_q \hat{b}_q = \sqrt{\kappa}\hat{a}_{\text{in}} + \frac{\kappa}{2}\hat{a} + \frac{\kappa}{2}\frac{\tilde{B}}{2}\frac{\hat{x}_m}{x_0}\hat{a} - \frac{\kappa}{4}\left(\frac{\tilde{B}}{2}\right)^2\frac{\hat{x}_m^2}{x_0^2}\hat{a}, \tag{B.14}$$

and substitute this into the equation of motion of the cavity mode,

$$\begin{aligned}\dot{\hat{a}} &= i\left[\hat{\mathscr{H}}_2, \hat{a}\right] \\ &= -i\left(\omega_c - \tilde{A}\kappa\frac{\hat{x}_m}{x_0}\right)\hat{a} - \sqrt{\frac{\kappa}{2\pi\rho}}\left[1 + \frac{\tilde{B}}{2}\frac{\hat{x}_m}{x_0} - \frac{1}{2}\left(\frac{\tilde{B}}{2}\right)^2\frac{\hat{x}_m^2}{x_0^2}\right]\sum_q\hat{b}_q \\ &= -i\left(\omega_c - \tilde{A}\kappa\frac{\hat{x}_m}{x_0}\right)\hat{a} - \left[1 + \frac{\tilde{B}}{2}\frac{\hat{x}_m}{x_0} - \frac{1}{2}\left(\frac{\tilde{B}}{2}\right)^2\frac{\hat{x}_m^2}{x_0^2}\right]\left[\sqrt{\kappa}\hat{a}_{\text{in}} + \frac{\kappa}{2}\hat{a} + \frac{\kappa}{2}\frac{\tilde{B}}{2}\frac{\hat{x}_m}{x_0}\hat{a} - \frac{\kappa}{4}\left(\frac{\tilde{B}}{2}\right)^2\frac{\hat{x}_m^2}{x_0^2}\hat{a}\right].\end{aligned} \tag{B.15}$$

Finally, all terms proportional to $\hat{x}_m^2\hat{a}$ cancel, i.e. the quadratic term in Eq. (1.6) drops out. The correct cavity equation of motion up to second order in $\hat{x}_m$ is given by

$$\dot{\hat{a}} = -i\left(\omega_c - \tilde{A}\kappa\frac{\hat{x}_m}{x_0}\right)\hat{a} - \sqrt{\kappa}\hat{a}_{\text{in}}\left[1 + \frac{\tilde{B}}{2}\frac{\hat{x}_m}{x_0} - \frac{1}{2}\left(\frac{\tilde{B}}{2}\right)^2\frac{\hat{x}_m^2}{x_0^2}\right] - \frac{\kappa}{2}\left[1 + \tilde{B}\frac{\hat{x}_m}{x_0} + \mathcal{O}(\hat{x}_m^3)\right]\hat{a} \tag{B.16}$$

instead. Note that a second order correction appears in combination with the optical input mode $\hat{a}_{\text{in}}$.

B.3. Steady-state solution of the classical equations of motion

In this section we investigate the pair of classical equations (1.11) and (1.12) that describe the mean values around which quantum fluctuations occur. We focus on the steady-state solution and show that, depending on the parameters, one to three solutions exist for purely dissipative coupling. Furthermore, we numerically solve the equations in presence of both dispersive and dissipative coupling.

In order to determine the steady-state solutions of Eqs. (1.11) and (1.12), we assume the drive strength Ω to be real. This can be done without loss of generality by shifting its phase to the intra-cavity amplitude $\bar{a}$. Then, focusing on purely dissipative coupling, i.e. $\tilde{A} = 0$, the classical equations of motion reduce to

$$0 = -\left(i\omega_m + \frac{\gamma}{2}\right)\bar{b} - i\tilde{B}\Omega\,\mathrm{Re}(\bar{a}) \tag{B.17}$$

$$0 = i\Delta\bar{a} - \left(1 + \frac{\tilde{B}}{2}\frac{\bar{x}}{x_0}\right)i\Omega - \left(1 + \tilde{B}\frac{\bar{x}}{x_0}\right)\frac{\kappa}{2}\bar{a}. \tag{B.18}$$

Equation (B.17) leads to

$$\bar{b} = \frac{-i\tilde{B}\Omega\,\mathrm{Re}(\bar{a})}{i\omega_m + \gamma/2}, \tag{B.19}$$

and allows to calculate the mean position $\bar{x}$ depending on the cavity amplitude $\bar{a}$,

$$\bar{x} = x_0(\bar{b} + \bar{b}^*) = x_0\left[\frac{-2\tilde{B}\Omega\,\mathrm{Re}(\bar{a})\omega_m}{\omega_m^2 + (\gamma/2)^2}\right] = -2x_0 z_B\frac{\Omega\,\mathrm{Re}(\bar{a})}{\tilde{B}}, \tag{B.20}$$

with $z_B = \frac{\tilde{B}^2\omega_m}{\omega_m^2 + (\gamma/2)^2}$ containing all properties of the mechanics. Substituting this into Eq. (B.18) leads to

$$\bar{a}\left\{[1 - 2z_B\Omega\,\mathrm{Re}(\bar{a})]\frac{\kappa}{2} - i\Delta\right\} = -[1 - z_B\Omega\,\mathrm{Re}(\bar{a})]\,i\Omega. \tag{B.21}$$

It is useful to split this equation into real and imaginary parts, resulting in

$$\mathrm{Re}(\bar{a})\left[1 - 2z_B\Omega\,\mathrm{Re}(\bar{a})\frac{\kappa}{2}\right] + \mathrm{Im}(\bar{a})\Delta = 0 \tag{B.22}$$

$$\mathrm{Im}(\bar{a})\left[1 - 2z_B\Omega\,\mathrm{Re}(\bar{a})\frac{\kappa}{2}\right] - \mathrm{Re}(\bar{a})\Delta = -\Omega + z_B\Omega^2\,\mathrm{Re}(\bar{a}). \tag{B.23}$$

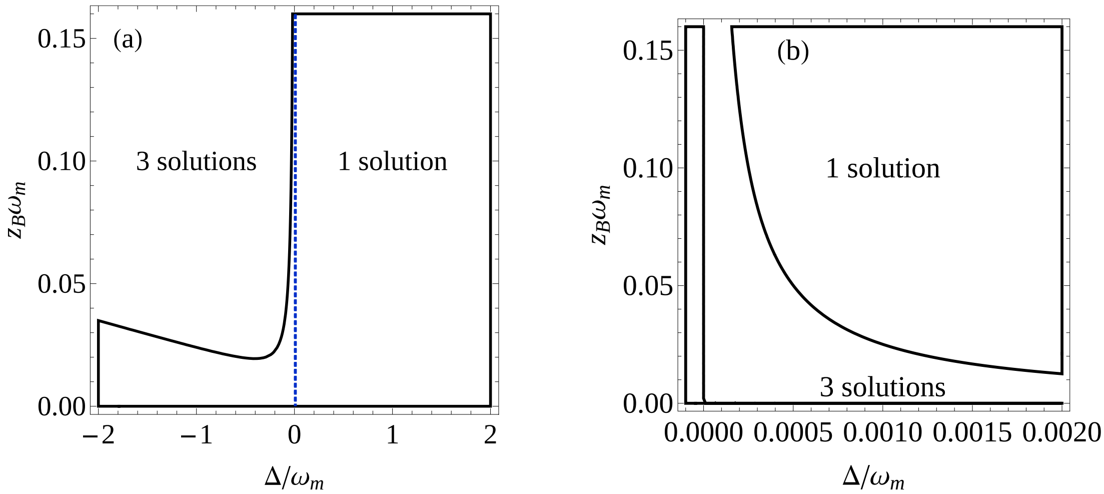

Figure B.1.: Number of real solutions to Eq. (B.25) as indicated by its discriminant. Parameters are $\omega_m/\kappa = 3$ and $\Omega/\omega_m = 10$. The region with three solutions, shown in (b) is not visible in (a) because it is too small. Its approximate location is indicated by the blue dashed line.

The first of these equations leads to

$$\operatorname{Im}(\bar{a}) = -\frac{[1 - 2z_B\Omega \operatorname{Re}(\bar{a})]\,\kappa}{2\Delta} \operatorname{Re}(\bar{a}). \tag{B.24}$$

Note that $\Delta = 0$ has to be treated separately. In this case a single solution is found, given by $\operatorname{Re}(\bar{a}) = 0$ and $\operatorname{Im}(\bar{a}) = -2\Omega/\kappa$.

If $\Delta \neq 0$, substituting Eq. (B.24) into Eq. (B.22) leads to

$$-\kappa^2 z_B^2 \Omega^2 \operatorname{Re}(\bar{a})^3 + \kappa^2 z_B \Omega \operatorname{Re}(\bar{a})^2 + \left[-(\kappa/2)^2 - \Delta^2 - z_B \Delta \Omega^2\right] \operatorname{Re}(\bar{a}) + \Omega\Delta = 0. \tag{B.25}$$

This is a third order polynomial in $\operatorname{Re}(\bar{a})$ and thus has one to three real solutions, depending on the coefficients. Both, $z_B = 0$ or $\Omega = 0$, simplify the equation such that it becomes linear in $\operatorname{Re}(\bar{a})$, thus leading to a single solution as it is expected. Furthermore, note that purely dispersive coupling leads to a polynomial of third order as well, but with respect to $|\bar{a}|^2$ rather than $\operatorname{Re}(\bar{a})$.

To investigate the number of solutions that correspond to different parameter sets, we determine the discriminant of Eq. (B.25). For an equation of the form $ax^3+bx^2+cx+d = 0$ it is given by $D = 18abcd - 4b^3d + b^2c^2 - 4ac^3 - 27a^2d^2$. If $D > 0$ three real solutions exist, if $D < 0$ there is one real solution in addition to two complex solutions. In the case of $D = 0$ all three solutions are real, but one is twofold. Figure B.1 shows the regions corresponding to either three or one real solution obtained from this criterion. We find two separate regions where three solutions exist, a large one at negative detuning Δ and a very narrow one at positive detuning. Whereas the large region, shown in Fig. B.1 (a),

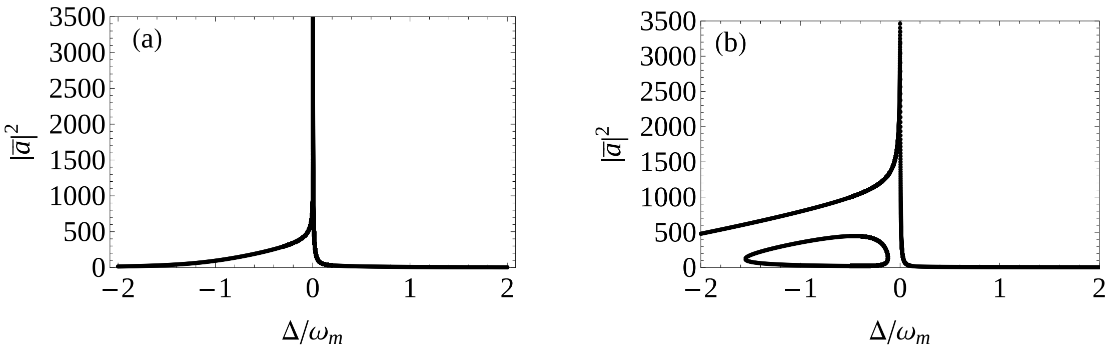

Figure B.2.: Number of photons inside the cavity $|\bar{a}|^2$ as a function of detuning Δ, for $\Omega/\omega_m = 5$ (a) and $\Omega/\omega_m = 10$ (b). Other parameters are $z_B\omega_m = 0.03$ (purely dissipative coupling, i.e. $\tilde{A} = 0$) and $\omega_m/\kappa = 3$.

increases with drive strength Ω, the smaller region, shown in Fig. B.1 (b), decreases for larger Ω.

Equation (B.25) can be solved exactly and from its solutions $\bar{a}$ and $\bar{x}$ can be determined. Figure B.2 shows the number of photons inside the cavity $|\bar{a}|^2$ as a function of detuning Δ. In absence of coupling, this is a Lorentzian. Applying purely dissipative coupling, the Lorentzian is modified with increasing drive strength Ω and finally a "bubble" opens up at negative detuning Δ. Notably, this differs from the bistable behaviour known for dispersive coupling (for an illustration of purely dispersive coupling, see below Fig. B.4 (a)). The effect of the small region with three solutions at positive detuning is not visible in this figure.

Remarkably, purely dissipative coupling leads to a mean position $\bar{x}$ that can be either positive or negative, depending on the detuning Δ, see Fig. B.3. This corresponds to the optical force being either attractive or repulsive, depending on Δ as it was observed in [18]. Recall, that purely dispersive coupling leads to $\bar{x} > 0$, corresponding to a repulsive radiation-pressure force.

To investigate the change of the steady-state behaviour for $\tilde{A} \neq 0$ we determine the steady-state solutions of the full equations (1.11) and (1.12). Assuming Ω to be real, as in the case of purely dissipative coupling, Eq. (1.11) leads to

$$\bar{b} = \frac{i\tilde{A}\kappa|\bar{a}|^2 - i\Omega\tilde{B}\,\mathrm{Re}(\bar{a})}{i\omega_m + \gamma/2}, \tag{B.26}$$

and thus

$$\bar{x} = x_0(\bar{b} + \bar{b}^*) = 2x_0\omega_m \frac{\tilde{A}\kappa|\bar{a}|^2 - \Omega\tilde{B}\,\mathrm{Re}(\bar{a})}{\omega_m^2 + (\gamma/2)^2}. \tag{B.27}$$

In addition to z_B we define the parameters z_A and z_{AB}, such that they contain the corresponding coupling strengths and the properties of the mechanical oscillator, $z_A = \frac{\tilde{A}^2\omega_m}{\omega_m^2+(\gamma/2)^2}$ and $z_{AB} = \frac{\tilde{A}\tilde{B}\omega_m}{\omega_m^2+(\gamma/2)^2}$. Using these parameters and inserting Eq. (B.27) into

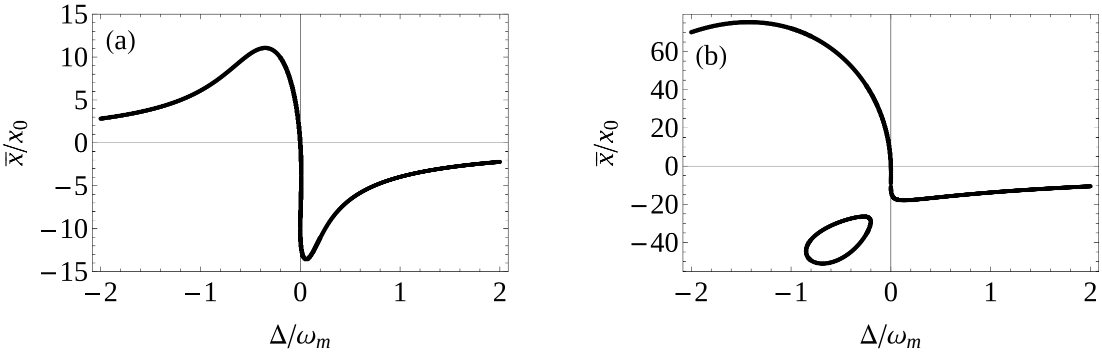

Figure B.3.: Mean position of the mechanical oscillator $\bar{x}$ as a function of detuning Δ for $\Omega/\omega_m = 5$ (a), and $\Omega/\omega_m = 15$ (b). Other parameters are $\omega_m/\kappa = 3$, $z_B\omega_m = 0.01$, and $\tilde{B} = 0.1$.

Eq. (1.12), we obtain

$$\begin{aligned} 0 &= i\left[\Delta + 2z_A\kappa^2|\bar{a}|^2 - 2\kappa\Omega z_{AB}\,\mathrm{Re}(\bar{a})\right]\bar{a} - i\Omega\left[1 + z_{AB}\kappa|\bar{a}|^2 - \Omega z_B\,\mathrm{Re}(\bar{a})\right] \\ &\quad - \frac{\kappa}{2}\bar{a}\left[1 + 2z_{AB}\kappa|\bar{a}|^2 - 2\Omega z_B\,\mathrm{Re}(\bar{a})\right]. \end{aligned} \tag{B.28}$$

Since this is a function of $\bar{a}$, $|\bar{a}|^2$ and $\mathrm{Re}(\bar{a})$, it is useful to express everything in terms of $\mathrm{Re}(\bar{a})$ and $\mathrm{Im}(\bar{a})$. Then we obtain

$$\begin{aligned} 0 &= i\left[\Delta + 2z_A\kappa^2\,\mathrm{Re}(\bar{a})^2 + 2z_A\kappa^2\,\mathrm{Im}(\bar{a})^2 - 2\kappa\Omega z_{AB}\,\mathrm{Re}(\bar{a})\right]\left[\mathrm{Re}(\bar{a}) + i\,\mathrm{Im}(\bar{a})\right] \\ &\quad - i\Omega\left[1 + z_{AB}\kappa\,\mathrm{Re}(\bar{a})^2 + z_{AB}\kappa\,\mathrm{Im}(\bar{a})^2 - \Omega z_B\,\mathrm{Re}(\bar{a})\right] \\ &\quad - \frac{\kappa}{2}\left[\mathrm{Re}(\bar{a}) + i\,\mathrm{Im}(\bar{a})\right]\left[1 + 2z_{AB}\kappa\,\mathrm{Re}(\bar{a})^2 + 2z_{AB}\kappa\,\mathrm{Im}(\bar{a})^2 - 2\Omega z_B\,\mathrm{Re}(\bar{a})\right], \end{aligned} \tag{B.29}$$

which is split into real and imaginary parts, leading to the coupled equations

$$\begin{aligned} 0 &= -\left[\Delta + 2z_A\kappa^2\,\mathrm{Re}(\bar{a})^2 + 2z_A\kappa^2\,\mathrm{Im}(\bar{a})^2 - 2\kappa\Omega z_{AB}\,\mathrm{Re}(\bar{a})\right]\mathrm{Im}(\bar{a}) \\ &\quad - \frac{\kappa}{2}\,\mathrm{Re}(\bar{a})(1 + 2z_{AB}\kappa\,\mathrm{Re}(\bar{a})^2 + 2z_{AB}\kappa\,\mathrm{Im}(\bar{a}) - 2\kappa\Omega z_B\,\mathrm{Re}(\bar{a})) \\ 0 &= \left[\Delta + 2z_A\kappa^2\,\mathrm{Re}(\bar{a})^2 + 2z_A\kappa^2\,\mathrm{Im}(\bar{a})^2 - 2\kappa\Omega z_{AB}\,\mathrm{Re}(\bar{a})\right]\mathrm{Re}(\bar{a}) \\ &\quad - \Omega\left[1 + z_{AB}\kappa\,\mathrm{Re}(\bar{a})^2 + z_{AB}\kappa\,\mathrm{Im}(\bar{a})^2 - \Omega z_B\,\mathrm{Re}(\bar{a})\right] \\ &\quad - \frac{\kappa}{2}\,\mathrm{Im}(\bar{a})\left[1 + z_{AB}\kappa\,\mathrm{Re}(\bar{a})^2 + 2z_{AB}\kappa\,\mathrm{Im}(\bar{a})^2 - 2\Omega z_B\,\mathrm{Re}(\bar{a})\right]. \end{aligned} \tag{B.30}$$

These equations can be solved numerically (e.g. using `NSolve[]` in Mathematica). Figure B.4 shows the results for different ratios of z_A and z_B, which corresponds to different ratios of dispersive ($\tilde{A}$) and dissipative ($\tilde{B}$) coupling strength. For purely dispersive ($z_B = 0$) coupling we find the known bistability at $\Delta < 0$, i.e. a tilted curve. Remarkably, adding dissipative coupling reduces the bistable region. If the dissipative coupling

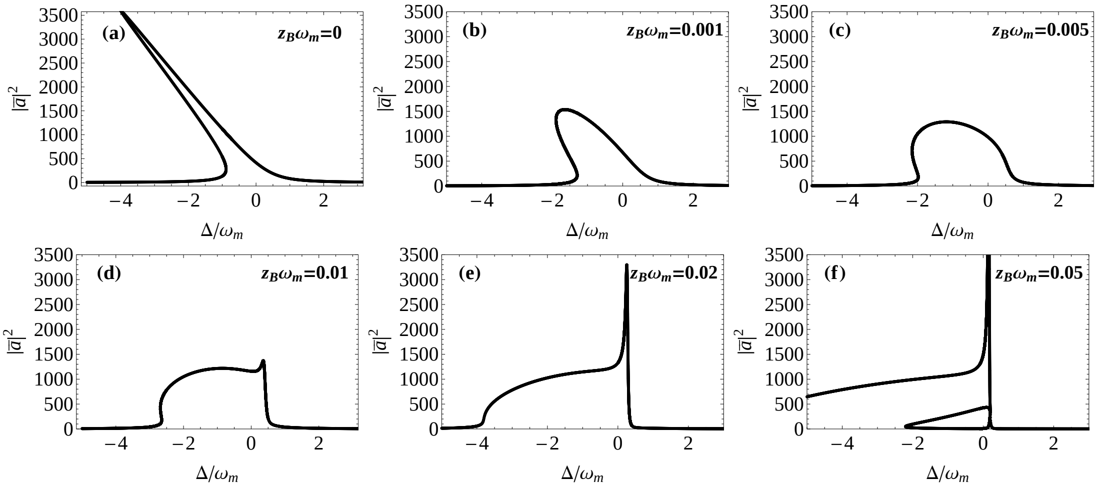

Figure B.4.: Mean number of photons inside the cavity $|\bar{a}|^2$, depending on the detuning Δ. (a)-(f) show different ratios of dispersive and dissipative coupling, i.e. $z_A\omega_m = 0.005$ is fixed and $z_B\omega_m$ varies from 0 to 0.05. Other parameters are $\Omega/\omega_m = 10$, $\omega_m/\kappa = 3$, and $z_{AB} = \sqrt{z_A}\sqrt{z_B}$.

strength exceeds the dispersive coupling strength , i.e. $z_B > z_A$, bistability vanishes until the typical behaviour of dissipative coupling dominates. Then three solutions exist for some values of Δ and the shape is comparable to the case of purely dissipative coupling, shown in Fig. B.2.

In addition to this description of the solutions of the classical equations of motion, a more systematic analysis of the situation is still to be done. The stability of the three solutions in the case of dissipative coupling needs to be determined. A careful and separate investigation of the two regions providing three solutions remains open. The purpose of this section is merely to summarize similarities (the existence of three solutions) and differences (two regions with three solutions, different line shape of $|\bar{a}|^2$ as a function of either Δ or Ω) of dispersive and dissipative coupling, and to indicate that it might be worthwhile to further investigate the classical equations.

B.4. Optically-induced frequency shift

The optical damping γ_{opt} and the optically-induced frequency shift $\delta\omega_m$ correspond to the imaginary and real part of the optomechanical self-energy $\Sigma(\omega)$, evaluated at the mechanical resonance frequency ω_m [8] (cf. Section 3.1). Applying a quantum noise approach allows to derive the optical damping from the weak-coupling force spectrum (see [22, 23] for the explicit calculation)

$$\gamma_{\text{opt}} = x_0^2 \left[S_{FF}(\omega_m) - S_{FF}(-\omega_m)\right]. \tag{B.31}$$

Thereby the connection of the frequency shift $\delta\omega_m$ to the force spectrum $S_{FF}(\omega)$ can be obtained with the help of the Kramers-Kronig relations, which is one goal of this section. Furthermore, we want to evaluate the expression for the optically-induced frequency shift $\delta\omega_m$ with the help of complex contour integration and the residue theorem, to show that the result is consistent with our definition of the optomechanical self-energy $\Sigma(\omega)$. For the mathematical principles used in this section, see e.g. Ref. [24].

Starting from

$$\Sigma(\omega_m) = \delta\omega_m - i\frac{\gamma_{\rm opt}}{2}, \tag{B.32}$$

without explicit knowledge of $\Sigma(\omega_m)$, the Kramers-Kronig relation yields

$$\mathrm{Re}[\Sigma(\omega_m)] = \frac{1}{\pi}\mathscr{P}\int d\omega' \frac{\mathrm{Im}[\Sigma(\omega')]}{\omega' - \omega_m}, \tag{B.33}$$

where $\mathscr{P}$ denotes the Cauchy principle value of the integral. Thus, the optically-induced frequency shift can be determined by integrating the optical damping,

$$\begin{aligned}\delta\omega_m &= \frac{1}{\pi}\mathscr{P}\int d\omega \frac{-\gamma_{\rm opt}/2}{\omega - \omega_m} = -\frac{x_0^2}{2\pi}\mathscr{P}\int d\omega \left(\frac{S_{FF}(\omega)}{\omega-\omega_m} - \frac{S_{FF}(-\omega)}{-\omega+\omega_m}\right)\\ &= x_0^2\mathscr{P}\int \frac{d\omega}{2\pi}\frac{S_{FF}(\omega)}{\omega_m - \omega} + x_0^2\mathscr{P}\int\frac{d\omega'}{2\pi}(-1)\frac{S_{FF}(\omega')}{\omega'+\omega_m}\\ &= x_0^2\mathscr{P}\int\frac{d\omega}{2\pi}S_{FF}(\omega)\left(\frac{1}{\omega_m-\omega} - \frac{1}{\omega_m+\omega}\right).\end{aligned} \tag{B.34}$$

Here, only a change of the integration variable is necessary to obtain the last equality, i.e. the formula used in Section 2.2.

To evaluate Eq. (B.34), we integrate the two terms separately. Inserting the expression for the weak-coupling force spectrum Eq. (2.3) into the first term, we find

$$x_0^2\mathscr{P}\int\frac{d\omega}{2\pi}S_{FF}(\omega)\frac{1}{\omega_m-\omega} = \mathscr{P}\int\frac{d\omega}{2\pi}\kappa\left(\frac{\tilde{B}|\bar{a}|}{2x_0}\right)^2\frac{1}{(\Delta+\omega)^2+(\kappa/2)^2}\left(\omega+2\Delta-\frac{2\tilde{A}\kappa}{\tilde{B}}\right)^2\frac{1}{\omega_m-\omega}. \tag{B.35}$$

From this we can read off the three poles of the integrand, i.e. they are at $\omega = \omega_m$ and $\omega = -\Delta \pm i\kappa/2$. The second term of Eq. (B.34) is given by

$$x_0^2\mathscr{P}\int\frac{d\omega}{2\pi}S_{FF}(\omega)\frac{1}{\omega_m+\omega} = \mathscr{P}\int\frac{d\omega}{2\pi}\kappa\left(\frac{\tilde{B}|\bar{a}|}{2x_0}\right)^2\frac{1}{(\Delta+\omega)^2+(\kappa/2)^2}\left(\omega+2\Delta-\frac{2\tilde{A}\kappa}{\tilde{B}}\right)^2\frac{1}{\omega_m+\omega}, \tag{B.36}$$

and has poles at $\omega = -\omega_m$ and $\omega = -\Delta \pm i\kappa/2$. Each of the integrands has a pole lying on the real axis, as well as a pole in the upper complex half-plane and a pole in the lower complex half-plane.

So far, by writing $\mathscr{P}\int d\omega f(\omega)$ we implicitly meant $\mathscr{P}\int_{-\infty}^{+\infty} d\omega f(\omega)$. Using complex contour integration, we can obtain this integral from

$$\mathscr{P}\int_{-\infty}^{\infty} d\omega f(\omega) = \mathscr{P}\oint_{\alpha} d\omega f(\omega) - \int_{\beta} d\omega f(\omega), \tag{B.37}$$

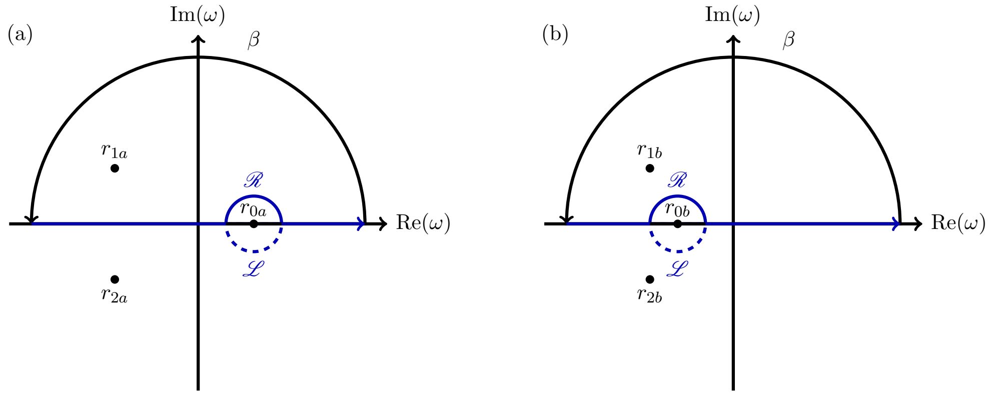

Figure B.5.: Illustration of the poles and integration paths used to evaluate (a) Eq. (B.35) and (b) Eq. (B.36).

where α denotes a path along the real axis that is closed e.g. with an arc across the upper half-plane. β denotes only that part of the closed path which doesn't lie on the real axis, i.e. in our case it is given by the arc. Integration from $-\infty$ to $+\infty$ implies that the radius of the arc has to be increased to infinity. Furthermore, we have to take into account that one of the poles lies on the real axis, thus we make use of the definition of the principal value as $\mathscr{P}\int d\omega f(\omega) = [\mathscr{L}\int d\omega f(\omega) + \mathscr{R}\int d\omega f(\omega)]/2$. Here $\mathscr{L}$ ($\mathscr{R}$) indicates that the integration path is modified using an infinitesimally small arc around the pole on the real axis, such that the pole lies on the left (right) side of the integration path, see Fig. B.5.

Thus Eq. (B.34) becomes

$$\frac{\delta\omega_m}{x_0^2} = \mathscr{P}\int_{-\infty}^{+\infty} \frac{d\omega}{2\pi} S_{FF}(\omega)\left(\frac{1}{\omega_m-\omega} - \frac{1}{\omega_m+\omega}\right)$$
$$= \frac{\mathscr{L}\oint\limits_{\alpha} \frac{d\omega}{2\pi}\frac{S_{FF}(\omega)}{\omega_m-\omega} + \mathscr{R}\oint\limits_{\alpha} \frac{d\omega}{2\pi}\frac{S_{FF}(\omega)}{\omega_m-\omega} - 2\int\limits_{\beta} \frac{d\omega}{2\pi}\frac{S_{FF}(\omega)}{\omega_m-\omega}}{2} - \frac{\mathscr{L}\oint\limits_{\alpha} \frac{d\omega}{2\pi}\frac{S_{FF}(\omega)}{\omega_m+\omega} + \mathscr{R}\oint\limits_{\alpha} \frac{d\omega}{2\pi}\frac{S_{FF}(\omega)}{\omega_m+\omega} - 2\int\limits_{\beta} \frac{d\omega}{2\pi}\frac{S_{FF}(\omega)}{\omega_m+\omega}}{2}. \tag{B.38}$$

The residue theorem allows to calculate the closed path integrals $\oint_\alpha f(\omega)d\omega = 2\pi i\sum_p \nu(p)\mathrm{Res}_p f$ by calculating and summing the residues of the enclosed poles, where $\nu(p)$ denotes the winding number of each pole p. In our case, the residues can be calculated using the theorem $f(\omega) = g(\omega)/h(\omega) \to \mathrm{Res}_p f = g(p)/h'(p)$. This can be applied if the function $f(\omega)$ consists of a numerator $g(\omega)$ and denominator $h(\omega)$ which are analytical functions and all its poles are simple poles. Since this is true for the functions considered here, we find

$$
\begin{aligned}
r_{0a} &= \frac{1}{x_0^2}\frac{\kappa|\bar{a}|^2\left[\tilde{B}(2\Delta+\omega_m)-2\tilde{A}\kappa\right]^2}{\kappa^2+4(\Delta+\omega_m)^2}\\
r_{1a} &= \frac{1}{x_0^2}\frac{\left(2\tilde{B}\Delta-4\tilde{A}\kappa+i\tilde{B}\kappa\right)^2|\bar{a}|^2}{8\left[2i(\Delta+\omega_m)+\kappa\right]}\\
r_{0b} &= \frac{1}{x_0^2}\frac{\kappa|\bar{a}|^2\left[\tilde{B}(-2\Delta+\omega_m)+2\tilde{A}\kappa\right]^2}{\kappa^2+4(\Delta-\omega_m)^2}\\
r_{1b} &= \frac{1}{x_0^2}\frac{i\left(2\tilde{B}\Delta-4\tilde{A}\kappa+i\tilde{B}\kappa\right)^2|\bar{a}|^2}{8\left[2(\Delta-\omega_m)-i\kappa\right]},
\end{aligned}
\tag{B.39}
$$

where we used $\nu(p)=1$ for all poles. The naming of the residues refers to Fig. B.5. Inserting this into Eq. (B.38) leads to

$$
\delta\omega_m = x_0^2\left[\frac{i\left(r_{0a}+r_{1a}+r_{1a}\right)-2\int_\beta \frac{d\omega}{2\pi}\frac{S_{FF}(\omega)}{\omega_m-\omega}}{2}-\frac{i\left(r_{0b}+r_{1b}+r_{1b}\right)-2\int_\beta \frac{d\omega}{2\pi}\frac{S_{FF}(\omega)}{\omega_m+\omega}}{2}\right],
\tag{B.40}
$$

and only the contribution of the arc is left to be determined. Note that in the case of purely dispersive coupling, i.e. $\tilde{B}=0$, the force spectrum $S_{FF}(\omega)$ simplifies considerably, such that $\frac{S_{FF}(\omega)}{\omega_m\pm\omega}$ is a function where the numerator is independent of ω and the denominator is a polynomial of third order. Hence, the contribution of the path β vanishes as its length, i.e. the arc radius ω, goes to infinity. Indeed, there is a theorem stating that if the polynomial order of the denominator is at least two plus the polynomial order of the numerator, the contribution of the arc always vanishes [24]. Unfortunately, dissipative coupling modifies the force spectrum $S_{FF}(\omega)$ such that the polynomial order of denominator and numerator differ only by one and we have to take the contribution of the integrations along β into account.

Using the parametrization $\beta(t)=\omega e^{it}$ of the path β, we find

$$
\begin{aligned}
\int_\beta \frac{d\omega}{2\pi}\frac{S_{FF}(\omega)}{\omega_m-\omega} &= \lim_{\omega\to\infty}\int_0^\pi \frac{dt}{2\pi}\frac{S_{FF}(\beta(t))}{\omega_m-\beta(t)}\dot{\beta}(t) = \int_0^\pi \frac{dt}{2\pi}\lim_{\omega\to\infty}\frac{S_{FF}(\beta(t))}{\omega_m-\beta(t)}i\omega e^{it}\\
&= \int_0^\pi \frac{dt}{2\pi}\left(-\frac{1}{4x_0^2}\tilde{B}^2|\bar{a}|^2\kappa\right) = -i\frac{\tilde{B}^2|\bar{a}|^2\kappa}{8x_0^2}.
\end{aligned}
\tag{B.41}
$$

An analogous calculation leads to

$$
\int_\beta \frac{d\omega}{2\pi}\frac{S_{FF}(\omega)}{\omega_m+\omega} = i\frac{\tilde{B}^2|\bar{a}|^2\kappa}{8x_0^2}.
\tag{B.42}
$$

Finally, we have calculated all contributions to the frequency shift and substituting Eqs. (B.41) and (B.42) into (B.40) leads to

$$\begin{aligned}\delta\omega_m &= x_0^2\left[\frac{ir_{0a}+2ir_{1a}-2\left(-i\frac{\tilde{B}^2|\bar{a}|^2\kappa}{8x_0^2}\right)}{2}-\frac{ir_{0b}+2ir_{1b}-2\left(i\frac{\tilde{B}^2|\bar{a}|^2\kappa}{8x_0^2}\right)}{2}\right]\\ &= i\frac{r_{0a}-r_{0b}}{2}+i\left(r_{1a}-r_{1b}\right)+\frac{i}{4}\tilde{B}^2|\bar{a}|^2\kappa\\ &= \mathrm{Re}[\Sigma(\omega_m)].\end{aligned} \tag{B.43}$$

The last equality can be explicitly checked using the definition of the optomechanical self-energy, Eq. (3.7). Its validity confirms our definition of $\Sigma(\omega)$.

B.5. OMIT approximation

To derive an approximation for the optical output signal that captures the OMIT behaviour, we neglect the contribution at the lower sideband, i.e. where $\delta = -\omega_m$. This requires to be in the good-cavity limit, where this contribution is off-resonant and thus negligible. If $\omega_m \gg \kappa$, we start from Eqs. (1.15) and (1.16) and drop the terms coupling to either $\hat{c}^\dagger$, $\hat{d}^\dagger$ or $\hat{\xi}_{\mathrm{in}}^\dagger$. Then, the approximate equations of motion are given by

$$\dot{\hat{c}} = -\left(i\omega_m+\frac{\gamma}{2}\right)\hat{c}-\sqrt{\gamma}\hat{\eta}+i\tilde{A}\kappa\bar{a}^*\hat{d}-\frac{\tilde{B}}{2}\sqrt{\kappa}\bar{a}^*\hat{\xi}_{\mathrm{in}}-\frac{\tilde{B}}{2}\left(i\Delta+\frac{\kappa}{2}\right)\bar{a}^*\hat{d} \tag{B.44}$$

$$\dot{\hat{d}} = i\Delta\hat{d}-\frac{\kappa}{2}\hat{d}-\sqrt{\kappa}\hat{\xi}_{\mathrm{in}}+\left[i\tilde{A}\kappa\bar{a}-\frac{\kappa}{2}\tilde{B}\bar{a}-\left(i\Delta-\frac{\kappa}{2}\right)\bar{a}\frac{\tilde{B}}{2}\right]\hat{c}. \tag{B.45}$$

Similar to the treatment of the exact equations of motion, we solve Eqs. (B.44) and (B.45) in Fourier space. Noticing that $\langle\hat{\eta}\rangle = 0$, we can readily drop this term in Eq. (B.44), since it cannot contribute to $\langle\hat{\xi}_{\mathrm{out}}\rangle$. We find

$$\chi_m^{-1}(\omega)\hat{c} = i\tilde{A}\kappa\bar{a}^*\hat{d}-\frac{\tilde{B}}{2}\bar{a}^*\left(i\Delta+\frac{\kappa}{2}\right)\hat{d}-\frac{\tilde{B}}{2}\sqrt{\kappa}\bar{a}^*\hat{\xi}_{\mathrm{in}}, \tag{B.46}$$

and

$$\hat{d} = -\sqrt{\kappa}\chi_c(\omega)\hat{\xi}_{\mathrm{in}}+\chi_c(\omega)\left[-\frac{\tilde{B}}{2}\left(i\Delta+\frac{\kappa}{2}\right)\bar{a}+i\tilde{A}\kappa\bar{a}\right]\hat{c}, \tag{B.47}$$

and substitute Eq. (B.47) into (B.46). Identifying $\alpha(\omega)$, cf. Eq. (3.8), this leads to

$$\chi_m^{-1}(\omega)\hat{c} = -\sqrt{\kappa}\bar{a}^*\alpha(\omega)\hat{\xi}_{\mathrm{in}}+\chi_c(\omega)\left[-\left(\tilde{A}\kappa|\bar{a}|\right)^2+\left(\frac{\tilde{B}}{2}\right)^2\left(i\Delta+\frac{\kappa}{2}\right)^2|\bar{a}|^2-i\tilde{B}\tilde{A}\kappa|\bar{a}|^2\left(i\Delta+\frac{\kappa}{2}\right)\right]\hat{c}. \tag{B.48}$$

Here, in the square brackets, we don't find the optomechanical self-energy, but only terms of it due to the approximation. In particular, the terms proportional to $\chi_c^*(-\omega)$ in the definition of $\Sigma(\omega)$, Eq. (3.7), are not reproduced. Defining $\tilde{\Sigma}(\omega) = \tilde{\Sigma}_{\tilde{A}}(\omega) + \tilde{\Sigma}_{\tilde{B}}(\omega) + \tilde{\Sigma}_{\tilde{A}\tilde{B}}(\omega)$ with components

$$\begin{aligned} \tilde{\Sigma}_{\tilde{A}}(\omega) &= -i(\tilde{A}\kappa|\bar{a}|)^2 \chi_c(\omega) \\ \tilde{\Sigma}_{\tilde{B}}(\omega) &= i\left(\tfrac{\tilde{B}}{2}\right)^2 |\bar{a}|^2 \chi_c(\omega) \left(i\Delta + \tfrac{\kappa}{2}\right)^2 \\ \tilde{\Sigma}_{\tilde{A}\tilde{B}}(\omega) &= \tilde{B}\tilde{A}\kappa\, |\bar{a}|^2 \chi_c(\omega) \left(i\Delta + \tfrac{\kappa}{2}\right), \end{aligned} \tag{B.49}$$

leads to

$$\hat{c} = \frac{-\sqrt{\kappa}\bar{a}^* \alpha(\omega)}{\chi_m^{-1}(\omega) + i\tilde{\Sigma}(\omega)} \hat{\xi}_{\text{in}}, \tag{B.50}$$

and

$$\hat{d} = -\sqrt{\kappa}\chi_c(\omega)\hat{\xi}_{\text{in}} + \chi_c(\omega)\left[-\frac{\tilde{B}}{2}\left(i\Delta + \frac{\kappa}{2}\right)\bar{a} + i\tilde{A}\kappa\bar{a}\right] \frac{-\sqrt{\kappa}\bar{a}^*\alpha(\omega)}{\chi_m^{-1}(\omega) + i\tilde{\Sigma}(\omega)} \hat{\xi}_{\text{in}}. \tag{B.51}$$

Finally, substituting Eqs. (B.50) and (B.51) into the linearized input-output equation (3.12) where the term proportional to $\hat{c}^\dagger$ is neglected, i.e. $\hat{\xi}_{\text{in}} - \hat{\xi}_{\text{out}} = -\sqrt{\kappa}\hat{d} - \sqrt{\kappa}\tilde{B}\bar{a}\hat{c}/2$, the output mode in Fourier space is given by

$$\begin{aligned} \hat{\xi}_{\text{out}} &= \hat{\xi}_{\text{in}} + \sqrt{\kappa}\hat{d} + \sqrt{\kappa}\frac{\tilde{B}}{2}\bar{a}\hat{c} \\ &= \left\{1 - \kappa\chi_c(\omega) - \frac{\kappa\chi_c(\omega)\bar{a}^*\alpha(\omega)\left[-\frac{\tilde{B}}{2}\left(i\Delta + \frac{\kappa}{2}\right)\bar{a} + i\tilde{A}\kappa\bar{a}\right]}{\chi_m^{-1}(\omega) + i\tilde{\Sigma}(\omega)} - \frac{\kappa\frac{\tilde{B}}{2}|\bar{a}|^2}{\chi_m^{-1}(\omega) + i\tilde{\Sigma}(\omega)}\right\}\hat{\xi}_{\text{in}} \\ &= \left[1 - \kappa\chi_c(\omega) - \frac{\kappa|\bar{a}|^2\alpha(\omega)^2}{\chi_m^{-1}(\omega) + i\tilde{\Sigma}(\omega)}\right]\hat{\xi}_{\text{in}}. \end{aligned} \tag{B.52}$$

To investigate the OMIT signal, we calculate the expectation value $\langle\hat{\xi}_{\text{out}}(t)\rangle$ in the time domain. Due to the probe laser, the expectation value of the input mode in Fourier space is given by $\langle\hat{\xi}_{\text{in}}(\omega)\rangle = 2\pi\delta(\omega - \delta)\bar{d}_{\text{probe}}$. This leads to

$$\begin{aligned} \langle\hat{\xi}_{\text{out}}(t)\rangle &= \int_{-\infty}^{+\infty} \frac{d\omega}{2\pi} \langle\hat{\xi}_{\text{out}}(\omega)\rangle e^{-i\omega t} \\ &= \int_{-\infty}^{+\infty} \frac{d\omega}{2\pi}\left[1 - \kappa\chi_c(\omega) - \frac{\kappa|\bar{a}|^2\alpha(\omega)^2}{\chi_m^{-1}(\omega) + i\tilde{\Sigma}(\omega)}\right]\langle\hat{\xi}_{\text{in}}(\omega)\rangle e^{-i\omega t} \\ &= \left[1 - \kappa\chi_c(\delta) - \kappa\frac{|\bar{a}|^2\alpha(\delta)^2}{\chi_m^{-1}(\delta) + i\tilde{\Sigma}(\delta)}\right]\bar{d}_{\text{probe}} e^{-i\delta t} \\ &= A^-_{\text{approx}} e^{-i\delta t}, \end{aligned} \tag{B.53}$$

where we identified the approximate negative frequency amplitude Eq. (4.4). Since there is no positive frequency part we conclude $A^+_{\text{approx}} = 0$.

Bibliography

[1] P. Meystre, "A short walk through quantum optomechanics," *arXiv:1210.3619*, 2012.

[2] D. Kleckner and D. Bouwmeester, "Sub-kelvin optical cooling of a micromechanical resonator," *Nature*, vol. 444, p. 75, 2006.

[3] J. D. Teufel, T. Donner, D. Li, J. W. Harlow, M. S. Allman, K. Cicak, A. J. Sirois, J. D. Whittaker, K. W. Lehnert, and R. W. Simmonds, "Sideband cooling of micromechanical motion to the quantum ground state," *Nature*, vol. 475, p. 359, 2011.

[4] E. Verhagen, S. Deléglise, S. Weis, A. Schliesser, and T. J. Kippenberg, "Quantum-coherent coupling of a mechanical oscillator to an optical cavity mode," *Nature*, vol. 482, p. 63, 2012.

[5] T. J. Kippenberg and K. J. Vahala, "Cavity-optomechanics: Back-action at the mesoscale," *Science*, vol. 321, p. 1172, 2008.

[6] F. Marquardt and S. M. Girvin, "Optomechanics," *Physics*, vol. 2, p. 40, May 2009.

[7] M. Aspelmeyer, S. Gröblacher, K. Hammerer, and N. Kiesel, "Quantum optomechanics—throwing a glance [invited]," *J. Opt. Soc. Am. B*, vol. 27, pp. A189–A197, 2010.

[8] F. Marquardt, J. P. Chen, A. A. Clerk, and S. M. Girvin, "Quantum theory of cavity-assisted sideband cooling of mechanical motion," *Phys. Rev. Lett.*, vol. 99, p. 093902, Aug 2007.

[9] I. Wilson-Rae, N. Nooshi, W. Zwerger, and T. J. Kippenberg, "Theory of ground state cooling of a mechanical oscillator using dynamical backaction," *Phys. Rev. Lett.*, vol. 99, p. 093901, Aug 2007.

[10] J. Chan, T. P. Mayer Alegre, A. H. Safavi-Naeini, J. T. Hill, A. Krause, G. S., M. Aspelmeyer, and O. Painter, "Laser cooling of a nanomechanical oscillator into its quantum ground state," *Nature*, vol. 478, p. 89, 2011.

[11] J. M. Dobrindt, I. Wilson-Rae, and T. J. Kippenberg, "Parametric normal-mode splitting in cavity optomechanics," *Phys. Rev. Lett.*, vol. 101, p. 263602, Dec 2008.

[12] S. Gröblacher, K. Hammerer, M. R. Vanner, and M. Aspelmeyer, "Observation of strong coupling between a micromechanical resonator and an optical cavity field," *Nature*, vol. 460, p. 724, 2009.

[13] G. S. Agarwal and S. Huang, "Electromagnetically induced transparency in mechanical effects of light," *Phys. Rev. A*, vol. 81, p. 041803, Apr 2010.

[14] S. Weis, R. Rivière, S. Deléglise, E. Gavartin, O. Arcizet, A. Schliesser, and T. J. Kippenberg, "Optomechanically induced transparency," *Science*, vol. 330, p. 1520, 2010.

[15] J. D. Teufel, D. Li, M. S. Allman, K. Cicak, A. J. Sirois, J. D. Whittaker, and R. W. Simmonds, "Circuit cavity electromechanics in the strong-coupling regime," *Nature*, vol. 471, p. 204, March 2011.

[16] F. Elste, S. M. Girvin, and A. A. Clerk, "Quantum noise interference and backaction cooling in cavity nanomechanics," *Phys. Rev. Lett.*, vol. 102, p. 207209, May 2009.

[17] A. Xuereb, R. Schnabel, and K. Hammerer, "Dissipative optomechanics in a michelson-sagnac interferometer," *Phys. Rev. Lett.*, vol. 107, p. 213604, Nov 2011.

[18] M. Li, W. H. P. Pernice, and H. X. Tang, "Reactive cavity optical force on microdisk-coupled nanomechanical beam waveguides," *Phys. Rev. Lett.*, vol. 103, p. 223901, Nov 2009.

[19] S. Huang and G. S. Agarwal, "Reactive coupling can beat the motional quantum limit of nanowaveguides coupled to a microdisk resonator," *Phys. Rev. A*, vol. 82, p. 033811, Sep 2010.

[20] S. Huang and G. S. Agarwal, "Reactive-coupling-induced normal mode splittings in microdisk resonators coupled to waveguides," *Phys. Rev. A*, vol. 81, p. 053810, May 2010.

[21] D. Walls and G. Milburn, *Quantum Optics*. Springer, 1994.

[22] A. A. Clerk, M. H. Devoret, S. M. Girvin, F. Marquardt, and R. J. Schoelkopf, "Introduction to quantum noise, measurement, and amplification," *Rev. Mod. Phys.*, vol. 82, pp. 1155–1208, Apr 2010.

[23] T. Weiß, "Sideband cooling in cavity optomechanics." Project Thesis.

[24] K. Jänich, *Analysis für Physiker und Ingenieure*. Springer, 4. ed., 1983.